PRECISE SIZE CONTROL AND NOISE REDUCTION OF SOLID-STATE NANOPORES FOR THE DETECTION OF DNA-PROTEIN COMPLEXES

ERIC BEAMISH

THESIS SUBMITTED IN PARTIAL FULFILLMENT OF THE REQUIRMENTS
FOR THE DEGREE OF

MASTER OF SCIENCE
in the Faculty of Graduate Studies (Physics)

UNIVERSITY OF OTTAWA

ABSTRACT

Over the past decade, solid-state nanopores have emerged as a versatile tool for the detection and characterization of single molecules, showing great promise in the field of personalized medicine as diagnostic and genotyping platforms. While solid-state nanopores offer increased durability and functionality over a wider range of experimental conditions compared to their biological counterparts, reliable fabrication of low-noise solid-state nanopores remains a challenge. In this thesis, a methodology for treating nanopores using high electric fields in an automated fashion by applying short (0.1-2 s) pulses of 6-10 V is presented which drastically improves the yield of nanopores that can be used for molecular recognition studies. In particular, this technique allows for sub-nanometer control over nanopore size under experimental conditions, facilitates complete wetting of nanopores, reduces noise by up to three orders of magnitude and rejuvenates used pores for further experimentation. This improvement in fabrication yield (over 90%) ultimately makes nanopore-based sensing more efficient, cost-effective and accessible.

Tuning size using high electric fields facilitates nanopore fabrication and improves functionality for single-molecule experiments. Here, the use of nanopores for the detection of DNA-protein complexes is examined. As proof-of-concept, neutravidin bound to double-stranded DNA is used as a model complex. The creation of the DNA-neutravidin complex using polymerase chain reaction with biotinylated primers and subsequent purification and multiplex creation is discussed. Finally, an outlook for extending this scheme for the identification of proteins in a sample based on translocation signatures is presented which could be implemented in a portable lab-on-a-chip device for the rapid detection of disease biomarkers.

STATEMENT OF ORIGINALITY

The content presented in this thesis is, to the best of the author's knowledge, the product of original work done by the author at the University of Ottawa under the supervision of Professor Michel Godin.

The majority of the content of chapters 4 and 5 of this thesis were accepted for publication in the journal *Nanotechnology* and was the result of collaboration of the four authors listed below. Similarly, the research presented in this paper for the enlargement and conditioning of solid-state nanopores using high electric fields was used in the application of a patent to secure intellectual property rights through the University of Ottawa.

> **Eric Beamish**, Harold Kwok, Vincent Tabard-Cossa and Michel Godin. *Precise Size Control and Noise Reduction of Solid-State Nanopores in Aqueous Solutions*. Nanotechnology (Accepted August, 2012).

As a partial requirement for the degree of Master of Science (Physics) at the University of Ottawa, enlarging and noise reduction research was presented at the Ottawa Carleton Institute of Physics symposium:

> **Eric Beamish** and Michel Godin. In situ *Size Control and Noise Reduction of Solid-State Nanopores*. Ottawa Carleton Institute of Physics (May 2012).

STATMEMENT OF CONTRIBUTIONS

All sample preparation, data acquisition and analysis presented in this thesis were performed by the author. Establishment of solid-state nanopore fabrication techniques was done with the help of Dr Yun Liu of the Centre for Catalysis Research and Innovation, who, with the author, drilled the majority of the nanopores used in experiments. Some of the nanopores used were also drilled by Harold Kwok. Many of the Labview routines used for data acquisition and analysis were modified versions of codes provided by Professor Vincent Tabard-Cossa of the University of Ottawa, while programs used for nanopore enlarging and subsequent analysis were co-written by the author and Lukasz Andrzejewski. Many tests for multiplex purification and gel analysis were also done by Jeremie Harris. With the exception of figures 1.1, 2.8, 3.1 and 3.3a, which were graciously provided by Professor Tabard-Cossa, and figures 2.1 and 2.6 which were done with the help of Stephanie Boudreau, all figures and plots were original work done by the author unless otherwise denoted.

CONTENTS

LIST OF FIGURES

LIST OF TABLES

ACKNOWLEDGEMENTS

First and foremost, I offer my sincerest gratitude to Professor Michel Godin whose guidance, patience and expertise contributed tremendously to my Master's experience. His ability to support students while allowing them freedom to work in their own way is a shining example of how a supervisor can both inspire and create a positive work environment.

A special thank you also to Professor Vincent Tabard-Cossa, without whose expertise and willingness to always offer support through discussion or a helping hand this work could not have been done. I would also like to thank the other members of my committee, Professor Andrew Pelling and Professor Manuella Vincter.

My Master's experience has taught me that no research is the work of one person, but the sum of countless contributions from many collaborators. I must thank Jason Riordon, whose patient help was instrumental in all aspects of my work in the lab, from setting up electronic systems to useful discussions about data analysis and interpretation (although in the end we never won the car). Jeremie Harris, too, was a tremendous help in preparing samples, testing protocols and running experiments. Special thanks also to Dr. Maryam Mirzaei, Radin Tahvildari, Nicolas Catafard and all of my other lab mates for helpful discussions and making the lab a fun and interesting place to work every day.

Most importantly, thanks to Mom, Scott and Kayla, this thesis could not have been completed without your unwavering support and encouragement. Stephanie, while we see your hand in some figures, your contributions are too numerous to mention. No one could ask for a better support network than you guys, thank you!

This thesis is dedicated to Granny and Stan. Thank you so much for your love and support, for your passion for life and family. Thank you for stories over dirty dishes at dinner and memories of even dirtier sap pails. Thank you for always being at every game and your daily calls to tell us just how great we are. Thank you for everything.

1 INTRODUCTION

Recent decades have shown increased interest in the provision of targeted healthcare. In such personalized medicine, biochemical measurements of an individual's blood glucose, presence or absence of proteins in a tissue sample and unique genetic code can be used to determine the best possible healthcare for that person. Personalized medicine tailored to a patient's genetic makeup, or genotype, shows particular promise of improving diagnosis and treatment, maximizing drug efficacy while minimizing harmful side effects and identifying genetic risk factors for the early screening and prevention of diseases and genetic disorders.

In human beings, the vast majority of DNA is made of up the same genetic sequence. Variation between individuals arises naturally from variations in genes and single nucleotide polymorphisms (SNPs). SNPs, which are single base pair differences at specific locations of the DNA sequence, can be translated to variations in the protein levels associated with specific diseases (biomarkers). Such biomarkers can be linked to an individual's predisposition to certain illnesses,[1,2] development of disease[3] and response to drug therapy.[4] For example, various treatment options for a particular condition can be stratified so that they are prescribed to patients who are most likely to respond. In the case of breast cancer victims, patients exhibiting high expression of the HER2 gene have shown increased response to the chemotherapeutic drug Herceptin.[5] Alternatively, where illnesses do not appear as a well-defined set of symptoms, genetic tests can be used to diagnose the disease, an approach that is currently used for muscular dystrophy.[6]

Although already showing great promise, personalized medicine through genotyping and the identification of biomarkers is in its infancy. At present, it is limited to cases where

the relationships between an individual's phenotype and genotype (i.e. SNPs), as well as between genotype and treatment response is well understood. The primary challenge facing advancement in the field is the cost associated with determining an individual's genetic sequence and limited knowledge of the association between pathogenesis and biomarker expression. For example, existing genotyping platforms require expensive and lengthy procedures of sample purification, fluorescent labeling and amplification. As such, cheaper and more rapid large-scale biomarker identification platforms are required to realize the goals of early disease detection and prevention as well as improved drug development and therapeutic response.

Over the past twenty years, nanopore sensing platforms have emerged as an attractive alternative to traditional methods of genetic sequencing and protein detection.[7] As they rely solely on translating the properties or activity of an individual molecule into an electrical signal, nanopores offer a high throughput, label-free method of detection and characterization of single molecules at low cost with minimal sample preparation. A nanopore system consists of a nanometer-sized hole in a thin insulating membrane separating two liquid electrolyte reservoirs. Sensing relies on providing an electrical readout of a molecule's activity as it is confined in the nano-scale geometry of the pore.[8,9] The first nanopores used to detect polymers were biological in nature,[10] the most common of which is α–hemolysin. Such nanopores are typically embedded in a lipid bilayer as shown in figure 1.1a, mimicking the protein channels found naturally in cell membranes. Since the first nanopore experiments, however, a wide host of applications for both biological and solid-state nanopores have been developed.[11] While biological pores offer precise structure and the capability of site-directed mutagenesis for highly reproducible, stable ionic current

measurements, controlled translocation speed and molecular specificity,[12] their fragility and fixed size limit their range of application. Solid-state nanopores, shown in figure 1.1b, on the other hand, offer increased durability over a wider range of experimental conditions and tuneable geometry.[13] These are also more naturally integrated into microfluidic and CMOS technologies for more precise fluidic and electronic control.[14,15]

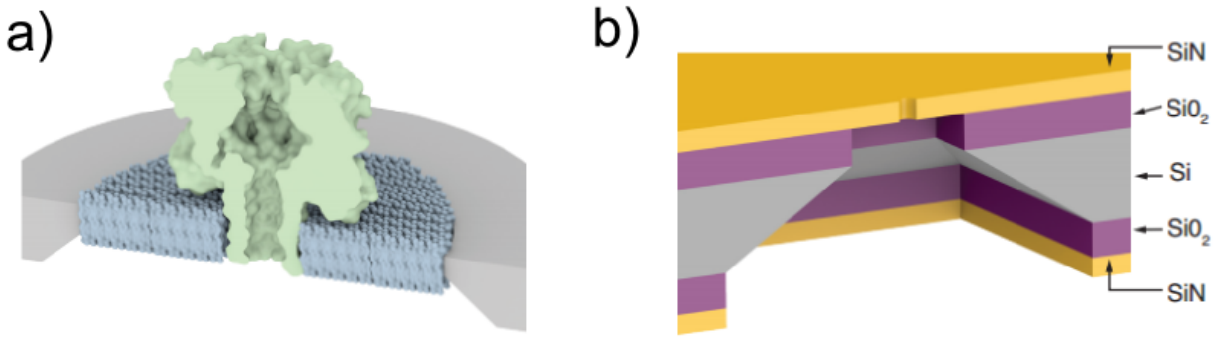

Figure 1.1 Cross-sectional views of (a) an α-hemolysin nanopore spanning a lipid bilayer membrane and (b) a solid-state nanopore fabricated in a thin insulating membrane.

Both biological and solid-state nanopore sensors rely on the Coulter principle, where single molecules are detected as characteristic current signatures as they traverse the nanopore channel.[16] When a potential bias is applied across the nanopore, an ionic current is measured. As a charged biomolecule such as DNA is electrophoretically driven through the nanopore, it displaces ions resulting in a current blockade that is proportional to the volume of the DNA strand. The properties of this current blockade, such as its shape, depth and duration can be used to extract information about the molecule's length, shape, charge and conformation.[13] The principle of their operation is illustrated in figure 1.2, where double-stranded DNA (dsDNA) passing through a nanopore in a folded configuration will exhibit a larger current blockade than that produced by linear dsDNA, as twice the volume of ions are displaced. The length of the molecule can also be determined from the duration of the event, as long molecules take more time to completely translocate through the pore.

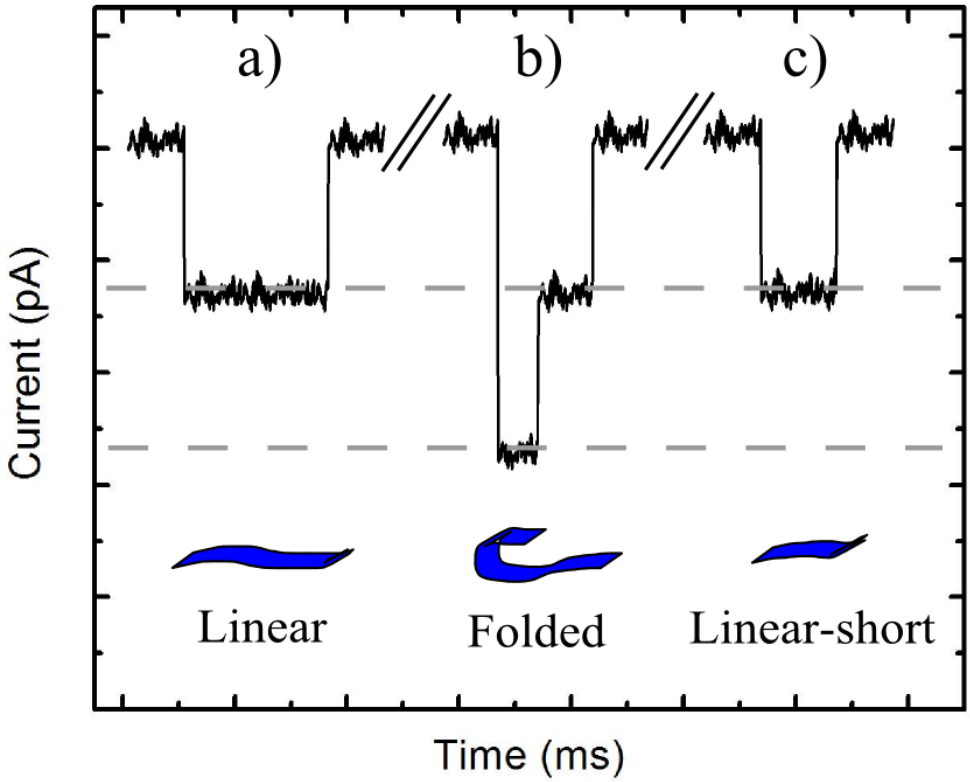

Figure 1.2 Current blockades characteristic of dsDNA translocation through a solid-state nanopore. Under an applied voltage bias, DNA molecules pass through the nanopore in a (a) linear or (b) folded configuration which can be identified by the depth of the current blockade. (c) The length of the DNA strand can be determined by the duration of the translocation event.

Nanopore sensing platforms have earned much attention due to their potential application as sequencing devices.[11] It is hoped that the genetic sequence of a translocating DNA strand could be determined from the electrical signal produced by each base as it passes through the nanopore. As such, the vast majority of nanopore experiments focus on the detection and characterization of DNA molecules. Most sequencing strategies have so far sought to increase sensitivity and slow the transport of DNA through the nanopore in order to improve electrical readout.[17–19] While temporal resolution and sufficient sensitivity to sequence the human genome in a rapid, high-throughput manner have not yet been realized, it is now possible to distinguish between the four bases comprising genetic material

using proteinaceous nanopores, showing great promise for nanopore sensing platforms for genotyping applications.[20]

Despite the attention given to nucleic acid analysis for sequencing applications, nanopores have proven to be valuable tools for other single-molecule studies. For instance, solid-state nanopores have been used in various force spectroscopy experiments for determining the strength of molecular interactions[21–23] as well as in the study of proteins[24–26] and DNA-protein interactions.[17,27–29] From the perspective of medical diagnostics, the ability to study a variety of biomolecules opens the door for the use of nanopores as means of identifying disease biomarkers such as proteins and antibodies. A nanopore-based diagnostic tool would offer various advantages, such as the ability to detect very low concentrations from small sample volumes.[11]

Despite rigorous investigations into the discovery of novel molecular disease biomarkers for early diagnosis, guidance of therapy and monitoring of disease progression, elucidation of discriminating biomarkers remains a challenge for conventional techniques.[30] The discovery of effective biomarkers is confounded in large part by the complexity of disease signatures,[31] deficiencies in biomolecule capture and quantification technologies[32] and the associated cost.[33] There are very few conditions which can be diagnosed by the presence of unique biomarkers, such as the prostate-specific antigen for prostate cancer.[34] More commonly, diseases produce heterogeneic chemical signatures that complicate diagnosis, resulting in a need for novel, high-throughput genomic techniques to better characterize disease biomarkers.[35] Conventional proteomics assays are typically performed using two-dimensional gel electrophoresis (2-DE), which has limited separation capabilities, is time consuming and has poor reproducibility.[32] Furthermore, 2-DE is often followed by

mass spectrometry analysis, which increases the cost and complexity of assays. Nanopore-based sensing platforms, on the other hand, would offer an attractive alternative, as they are high-throughput, extremely sensitive and relatively inexpensive in comparison to existing proteomics methods.

The noise and bandwidth limitations of solid-state nanopores currently prevent the direct identification of translocating proteins in an unknown sample; current technologies are mostly limited to detecting the presence or absence of translocating proteins.[26] Diagnosis from the translocation of disease biomarkers alone is therefore not yet feasible, as it is not possible to distinguish between the electrical signals produced from the many species found in a tissue sample. However, it is possible to conceive of a scheme whereby specific biomarkers can be isolated from a sample by taking advantage of the specificity of protein-antibody interactions and subsequently detected using a nanopore. One potential method of biomarker detection is discussed in chapter 6, where a hybrid DNA-protein complex could be used to isolate biomolecules of interest from a tissue sample and be distinguished by their characteristic current blockades in a nanopore sensor.

Realization of such a nanopore-based detection method is faced with several practical challenges. First of all, the small defined size of biological pores (<2 nm) prevents them from accommodating a bulky (10-30 nm) DNA-protein complex. On the other hand, while solid-state nanopores are capable of offering tuneability of size, reproducibly achieving pores of a desired diameter is extremely difficult and costly, as it requires lengthy drilling and treatment using specialized equipment such as a transmission electron microscope (TEM). Furthermore, solid-state nanopores exhibit significantly higher electrical noise and more rapid events than proteinaceous pores,[22] limiting their sensitivity as single-molecule

detectors. While severely limiting solid-state nanopore sensing platforms for medical diagnostic purposes, unreliable size control and lack of ability of reproducibly to obtain low-noise current traces plague virtually all solid-state nanopore applications. Combined with the fact that nanopores typically have a short lifespan and poor fabrication yield, nanopore experiments are both time consuming and costly. A method of reliably tuning solid-state nanopore size, improving the reproducibility of low-noise current signals and extending the nanopore lifetime is thus of paramount importance for improving the viability of solid-state nanopore sensing platforms.

This thesis presents a method of overcoming these challenges associated with solid-state nanopore research. While motivated by the goal of realizing the detection of DNA-protein conjugates for the identification of disease biomarkers, the protocol discussed is of great value in all solid-state nanopore applications. By applying short pulses of moderate voltage, a strong electric field is produced across the nanopore which can be used to remove surface atoms, offering sub-nanometer control over nanopore size, while simultaneously reducing signal noise in ionic current measurements. Furthermore, previously used nanopores with degraded electrical properties that would have otherwise been discarded can be subjected to high electric field pulses to regain ideal low-noise characteristics and can be reused for further experiment. Altogether, over 90% of nanopores conditioned using the technique described are capable of being used in molecular recognition experiments. With precise size control, increased yield and extended lifetime, the fabrication cost associated with solid-state nanopores is significantly reduced compared to untreated nanopores drilled with a TEM, ultimately making the sensing platform more accessible for a wider range of applications.

Chapter 2 details the method by which solid-state nanopores are fabricated in thin solid-state membranes using a transmission electron microscope (TEM). Currently the method of choice for the fabrication of sub-50 nm pores, the refined process as well as some of the challenges associated with the technique are discussed in detail. Chapter 3 discusses the prototype instrument design used for signal acquisition and provides a description of the methodology by which nanopores are mounted and characterized using low-noise current measurement techniques. The instrumentation used for the application of high electric field pulses to fine-tune size and condition nanopores for obtaining low-noise electrical signals is also introduced. An in-depth analysis of the size control and noise reduction capabilities of the technique is then presented in chapter 4, followed by an investigation of the functionality of conditioned nanopores in chapter 5, where DNA translocation was observed and used to characterize nanopore geometry. Finally, chapter 6 discusses the design of an experiment whereby a model protein, neutravidin, is bound to dsDNA as a proof-of-concept experiment for the detection of DNA-protein conjugates using solid-state nanopores. In order to improve temporal resolution, an analysis of DNA translocation in different electrolyte solutions is also discussed.

2 SOLID-STATE NANOPORE FABRICATION AND LIMITATIONS

In a nanopore experiment, the nanopore serves as the only conduit for ionic current between two reservoirs of electrolytic solution.[11] As the amplitude of the electrical signal produced from a translocating molecule is proportional to the ratio of the molecule's volume to the sensing volume of the nanopore,[36] for the investigation of biomolecules such as proteins or single- and double-stranded DNA, a nanopore must be on the order of 3-50 nm in diameter in order to distinguish events from background noise. In order to achieve such precision, solid-state nanopores are typically created using a tightly focused beam of highly energetic electrons in a transmission electron microscope (TEM),[37] as discussed in section 2.2. The resultant nanopore has a size and geometry dependent on the beam conditions and exposure time used in the drilling process,[38] as well as the properties of the membrane in which the nanopore is drilled. While this fabrication technique is now commonly used, several drawbacks exist that limit the effectiveness of solid-state nanopore sensing platforms. This section details the fabrication of solid state nanopores, as well as the challenges associated with their use that motivate the development of new methodology for preparing a solid-state nanopore for the detection of DNA-protein complexes.

2.1 Silicon nitride nanopore membranes

Silicon nitride is an ideal substrate in which to fabricate solid-state nanopores, as it is electrically insulating and can be easily manufactured. Commercially available membranes are typically created by depositing a given thickness of SiN on a silicon substrate and subsequently exposing a freestanding membrane window through KOH etching of the Si substrate. As such windows are useful for general purpose imaging of samples in a TEM, various vendors exist that offer similar products.

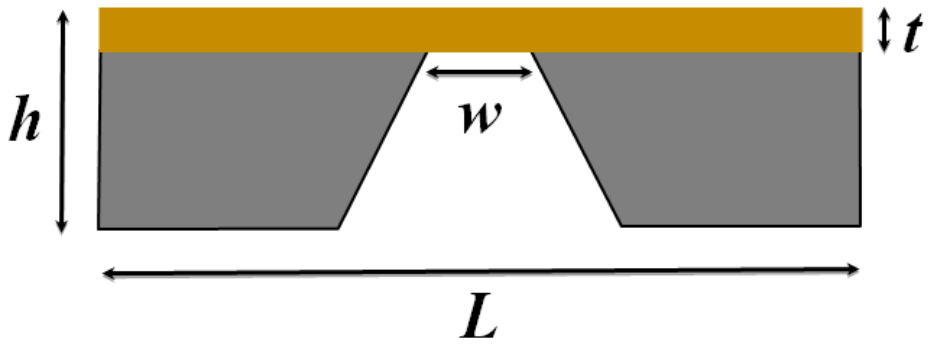

Figure 2.1 Schematic of a cross-section of a typical nanopore chip containing a SiN membrane (brown) of thickness t and window size w is supported on a Si support chip (gray) of length L and thickness h.

Figure 2.1 shows the schematic of a typical nanopore chip. A SiN membrane of thickness t and window size w is supported on a Si support chip of length L and thickness h. Since the amplitude of the current blockade ΔI of a translocating molecule is inversely proportional to the length of the nanopore, thin membranes are desirable in order to maximize the current signal. This relationship, derived from Ohm's law using the resistance of a cylindrical nanopore, is given by equations 2-1 and 2-2, where L_{pore} is the length of the nanopore, which for simplicity we assume to be the thickness of the membrane. While the signal amplitude is actually proportional the molecule to pore volume ratio, in practice this can be simplified to the ratio of the area of the pore containing a molecule to the open pore cross-sectional area when the molecules (such as long DNA strands) occupy the entire length of the pore.[22]

$$\frac{\Delta I}{I_{\text{open}}} = \frac{\Delta A_{\text{DNA}}}{A_{\text{pore}}} \qquad 2\text{-}1$$

$$\Delta I = \frac{\sigma V \Delta A_{\text{DNA}}}{L_{\text{pore}}} \qquad 2\text{-}2$$

Clearly, for a given voltage V, conductivity σ and change in pore volume upon translocation $\Delta A_{DNA,}$ decreasing membrane thickness increases the signal obtained from a translocating molecule. There are, however, practical limitations on how thin a membrane can be used. While some groups have used ultra-thin graphene membranes for very sensitive measurements,[39] for the purpose of this study it was found that sub-30 nm membranes were too fragile to manipulate without damaging the sample window. Similarly, large window sizes are also prone to breakage. Ultimately, 50 μm x 50 μm windows with a membrane thickness of 30 nm purchased from Norcada (NT005X, shown in figure 2.2) were found to be best suited for nanopore drilling and manipulation.

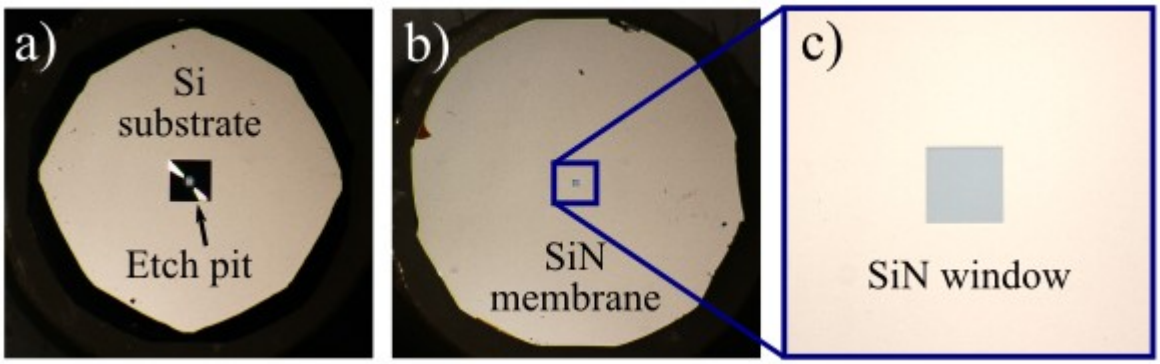

Figure 2.2 Optical images of the Norcada, Inc. membranes used. The silicon support chip contains an etched pit (a) through to the silicon nitride layer (b), exposing a silicon nitride membrane window (c). As denoted in the schematic of figure 2.1, t = 30 nm, w = 50 μm, L = 3 mm and h = 200 μm.

2.2 Nanopore drilling

Over the past ten years, the most common method of fabrication of solid-state nanopores with a desired diameter has been to tightly focus a beam of electrons on a thin membrane in a TEM.[37] When the electrons are accelerated to sufficient energies, removal of atoms from the membrane surface occurs through a sputtering process, leaving behind a pore whose size can be controlled with nanometer precision.

In order for sputtering to occur, incident electrons must have sufficient energy to overcome the binding energy of the surface atoms. This threshold energy in electron volts E_0 necessary for sputtering can be calculated from equation 2-3, where E_A is the binding energy of an atom with atomic mass number A.[40]

$$E_{\mathrm{A}}(\mathrm{eV}) = \frac{E_0}{(465.7\ \mathrm{eV})\ A}\left((1.02\ \mathrm{eV}) + \frac{E_0}{10^6}\right) \qquad 2\text{-}3$$

The sputtering rate S, or the rate at which atoms are removed from the membrane is dependent on the sputtering cross-section σ of the target atom, as shown by equation 2-4, where t_0 is the thickness of a single monolayer of atoms in the membrane and J/e is the current density of electrons per centimeter square per second.[41]

$$S = \frac{J}{e}\sigma t_0 \qquad 2\text{-}4$$

In substrates such as silicon nitride that contain more than one atomic species, it is possible for one element to be preferentially removed from the membrane surface, either due to a lower binding energy or more efficient energy transfer from the incident electron to the surface atom. Thus, over the course of sputtering, the membrane surrounding the nanopore formation region can become depleted of the species that is preferentially removed.[42] As it has been observed elsewhere that exposure to such conditions yields silicon-rich membranes, the sputtering of silicon is rate limiting in the creation of nanopores. Assuming a surface binding energy of 13 eV for silicon, equation 2-3 requires that incident electrons be of the order of ~150 keV.

In order to achieve the necessary incident electron energies and current densities for nanopore creation, a JEOL-2100F TEM was used. The schematic in figure 2.3 shows the ray diagram of the electron beam used in the drilling process for the various available

aperture angle settings. Here, the nanopore chip is mounted between the objective pre-field and post-field lenses. This model uses a thermal electron emission gun to produce electrons which are accelerated with a voltage of 200 kV for the purpose of nanopore drilling. When the beam passes through the sample, an image of the nanopore membrane is created on a fluorescent screen through the objective lens, which is used for the majority of beam alignment. The JEOL-2100F TEM used to drill pores offers three aperture angle settings (α_1, α_2, α_3). While all were used to create nanopores, it was found that α_3 (the largest aperture angle setting) was easiest to calibrate and provided the least amount of carbonaceous contamination following exposure to drilling conditions, likely due to increased current density on the membrane for more rapid drilling.

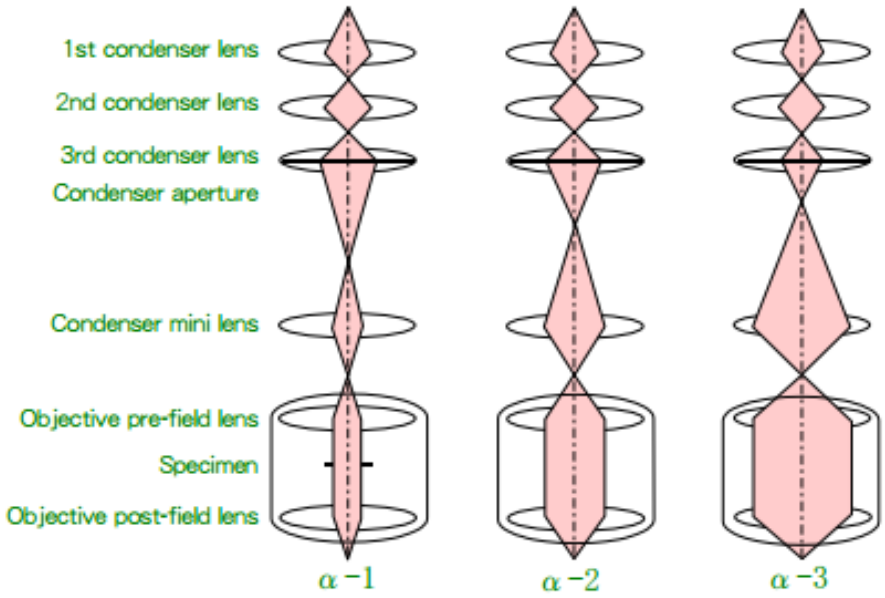

Figure 2.3 Ray diagram of the electron beam used for drilling nanopores. The nanopore chip is located between the objective pre-field and post-field lenses. The aperture angle setting of α_3 was provided optimal conditions for drilling while minimizing the amount of carbonaceous residue surrounding the resultant nanopore. Image adapted from the JEOL JEM-2100 operations manual.

The process of drilling a nanopore begins with mounting the nanopore chip on the TEM sample holder. The limited z-range focusing ability of the TEM means that the chip must be mounted membrane-side down. Due to the critical importance of voiding the sample chamber, a series of two vacuum pumps must be activated upon insertion of the sample holder into the TEM. Firstly, a rough evacuation is performed by an oil diffusion pump. After ~5 min of rough evacuation, the main vacuum system consisting of a turbo molecular pump is initiated by fully inserting the holder into the sample chamber. A final working pressure of the sample chamber is on the order of 10^{-5} Pa.

A nanopore is created using the 'TEM mode' of the JEOL-2100F. The membrane is first located and roughly centered on the fluorescent screen at low magnification (150 X) with both the condenser and objective apertures removed from the beam path. Magnification is then increased to 50 kX and the condenser aperture CL2 is inserted. The beam is then focused to a tight spot and centered using the aperture's *x* and *y* controls. If the membrane is not exactly in focus, then diffraction rings will appear on the fluorescent screen around the primary spot. The membrane can be roughly brought into focus by adjusting the z-height until the sample is brought into the focal plane, as indicated the disappearance of the diffraction rings.

The magnification is then increased to 600 kX, which is that used for drilling a nanopore. Once again, the beam is focused to a tight spot and centered on the fluorescent screen. At increased magnification, the sample can be more precisely brought into the focal plane by again adjusting the z-height of until diffraction rings disappear. It is also important at this stage to obtain a tight, symmetric bright spot by adjusting the condenser lens stigmator coil current using the "Cond Stig" controls, correcting and condenser lens

astigmatism. If the spot appears blurry, it may be necessary to reduce magnification and repeat the alignment procedure or adjust the focus knob. It is imperative however that the beam not remained condensed for too long, as this can initiate sputtering and subsequent thinning of the membrane.

In order to obtain an image of the membrane before drilling, the objective lens is inserted and centered on the fluorescent screen. The beam is then spread to < 10 pA/cm^2 and the CCD camera is inserted below the sample. Images are obtained using a EW500 CCD camera and are displayed on a computer monitor. When the membrane is viewed on the screen, a fast Fourier transform (FFT) of the image can be produced using ImageJ software, which can then be used to remove any objective lens astigmatism by adjusting deflection until the circular halo is completely round. Additionally, the sample can be brought into focus by tuning the focus knobs on the control panel until the diffraction rings expand to infinity.

Once the sample is properly aligned, a wait period is given to allow the sample to stop drifting with respect to the beam, which can be monitored on screen. The amount of time required for the image to stop drifting can vary substantially from sample to sample. Longer wait times of ~15 min are usually required for the first sample mounted in a day while the stage and apertures are still settling. By the third and fourth samples mounted, as little as 5 min can be sufficient for drifting to be reduced enough for drilling. At this point, the image can be refocused as needed and the camera removed. A CCD image of a properly focused membrane is shown in figure 2.4a.

To begin drilling, the beam is condensed to the smallest possible spot size. By following the steps outlined above, a nanopore will typically be created by waiting 45 s from

the time at which the beam was focused. However, it was observed that simply waiting for a certain amount of time did not yield reproducible nanopore sizes and in some cases did not produce a nanopore at all. This is likely a result of the difficulty of exactly aligning the sample in the focal plane and obtaining a perfectly symmetric spot size and focus to maximize the current density at the membrane. Additionally, variations in the membrane thickness from sample to sample can affect the amount of exposure time necessary to completely drill through the membrane.

Rather than waiting a set amount of time, a new procedure was developed in which the current density was monitored during the drilling process. When the beam is condensed on the membrane at the onset of drilling, a typical current density reading measured at the fluorescent screen is ~290-300 pA/cm^2. As the drilling progresses, the current density steadily rises until it has increased by ~18-25 pA/cm^2, at which point it plateaus when the membrane has been completely drilled through. Using this technique, nanopores between 3-13 nm in diameter can be created, as shown in figure 2.4b-d. Due to the brightness of the beam spot and the fact that the current density is continuously increasing as membrane material is being removed, it is very difficult to determine exactly at which point the nanopore is created. Unless the beam is expanded before a plateau is observed in the current density reading, the final nanopore size is dependent on the spot size used in the drilling process.

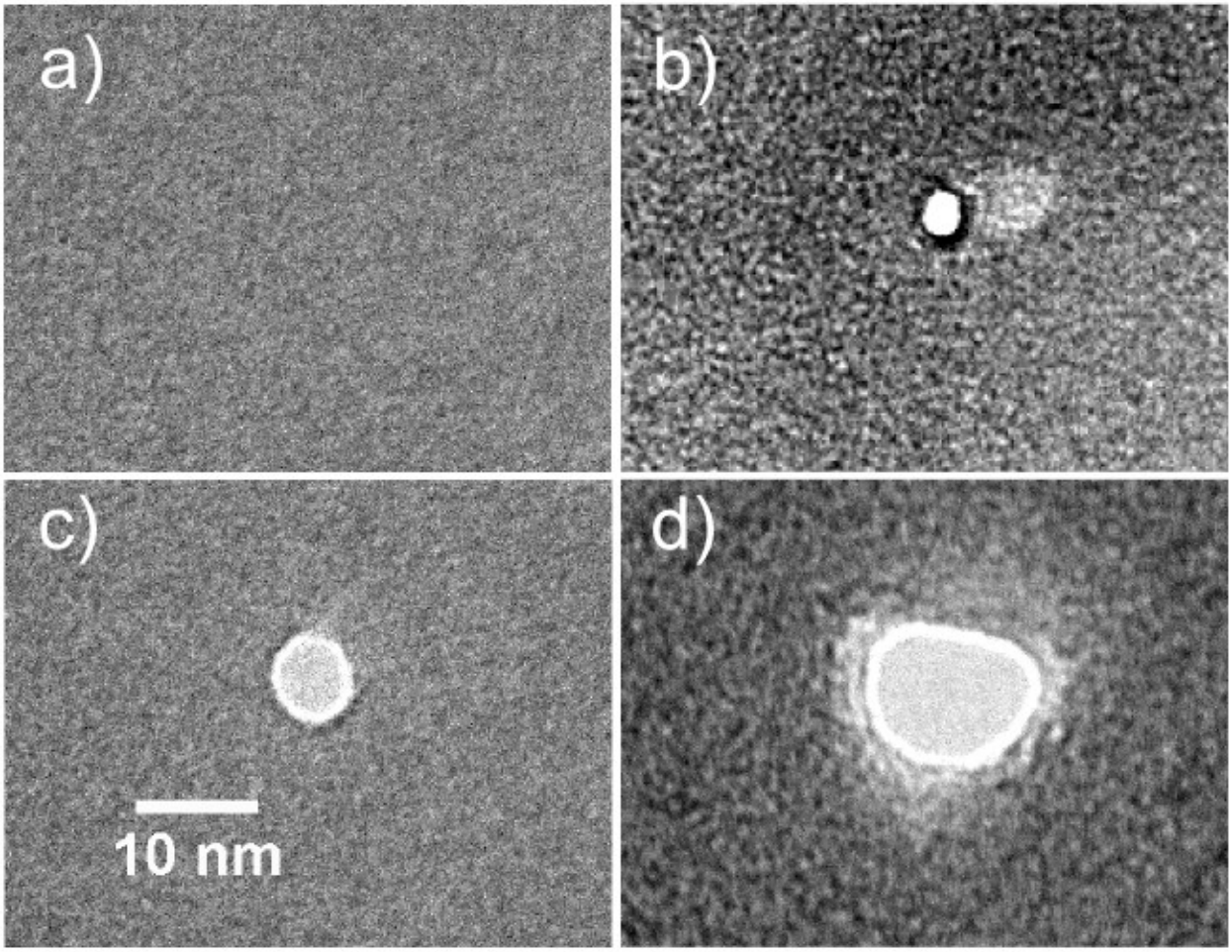

Figure 2.4 Examples of nanopores with various diameters created using the nanopore drilling technique described. (a) Shows a blank membrane immediately before drilling a nanopore. (b) Is a 3 nm diameter pore, (c) a 7 nm diameter pore and (d) a 13 nm diameter pore.

2.3 Challenges and limitations of solid-state nanopores

Despite the advantages of solid-state nanopores over their biological counterparts, there are various factors limiting their usefulness as single molecule sensors. While some of these limitations are inherent in the properties of solid-state nanopores themselves, there are also practical challenges involved in reproducibly creating and preparing a nanopore for experiment. Ultimately, these challenges drastically reduce the yield of nanopores that can actually be used in a biomolecular experiment, increasing the time and cost associated with

their fabrication as well as reducing their functionality for many potentially useful biological applications.

2.3.1 Reproducibility of solid-state nanopore drilling by TEM

The use of a TEM and similar drilling procedure to that described above is commonly accepted as the method of choice for the creation of solid-state nanopores.[11,13] Despite its broad usage, it is subject to several drawbacks that make it a less than ideal fabrication method.[22]

Most important is the fact that it is very difficult to reproducibly obtain nanopores of a particular size and shape using standard TEM drilling techniques. As the beam shape is essential in controlling the geometry of the resultant nanopore,[38] variations in the alignment of the nanopore membrane with the focal plane of the microscope and precise elimination of astigmatism are crucial in reproducibly creating nanopores. The entire process detailed above, however, is subjective and relies on the ability of a skilled user to properly align and focus the beam upon the introduction of each individual membrane. As the TEM beam conditions can vary over the course of a single drilling process, the result is that no two nanopores are identical.

Figure 2.5 highlights some of the challenges involved in reproducibly creating solid-state nanopores. Ideal nanopores created using the described drilling process are small and circular with well-defined edges. However, if insufficient time has been allowed for minimization of stage drift, or the electron beam is deflected due to charging of the membrane or apertures, it is possible to obtain nanopores that are elongated, with thinned regions tracing the path of the drift or deflection, as shown in figure 2.5a. Similarly, if the

stage drift is too rapid, the electron beam may simply trace the path of the drift without ever completely drilling through the membrane.

If the beam is not properly focused on the membrane, or if astigmatism is severe due to changes in the magnetization of the lenses or charging of the apertures as they are adjusted, it is possible to obtain oddly shaped pores or pores with unpredictably thinned edges. An example of this is shown in figure 2.5b, where one wall of the nanopore is a sharp edge and the other shows thinning of the membrane. Improper focusing can also lead to parasitic carbonaceous deposits on the surface on the surface of the membrane.[43] This occurs when the improperly focused beam contains insufficient energy to sputter membrane atoms at an appreciable rate, but can catalyze the reaction of membrane material with carbon compounds in the sample chamber. This contamination can be seen as dark patches of a CCD image of the membrane after a drilling attempt. When this occurs, it is often necessary to return to a low magnification and being the process of aligning and focusing the beam in a new location on the membrane, increasing the time required for fabrication. However, it is practically very difficult to create a nanopore that is completely free carbon contaminants. Such deposits can render the surface of the nanopore hydrophobic, which can impede complete wetting and complicate signal analysis, as discussed in section 2.3.3.

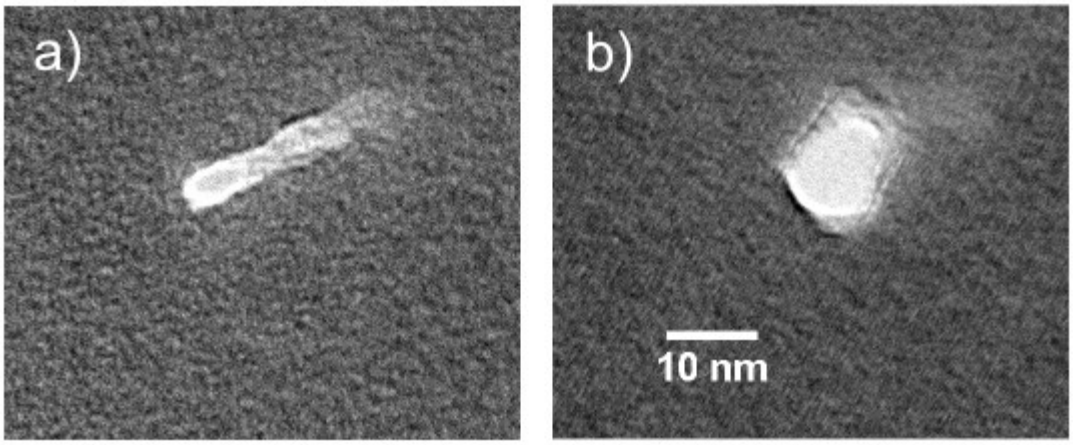

Figure 2.5 (a) Image of an elongated nanopore subjected to stage or beam drift. (b) Improper focusing of the electron beam while drilling lead to oddly thinned nanopore walls.

These issues can enormously increase the amount of time required to create nanopores in a reproducible manner. Considering the cost associated with TEM use and often its lack of availability, this can greatly limit the amount of nanopores that can be produced.

2.3.2 Control of nanopore size

Accurate control over nanopore size is crucial for their application as single molecule sensors. Not only does the size of a nanopore dictate the range of molecules that can be investigated, but also how sensitive of a detector it can be in terms of a molecule's conformation, size and activity.[44] In some specialized applications such as force spectroscopy, it is often necessary to have extreme control over nanopore size, so as to allow one molecular species to translocate but to be too small to allow the passage another.[22] For the purpose of detecting DNA-protein conjugates, however, the goal is to produce large enough nanopores to accommodate a very large complexes (15-25 nm in diameter) while still maintaining a high degree of sensitivity for detecting proteins bound along a DNA

scaffold. However, as described above, it is difficult to reproducibly achieve nanopores of a desired diameter using conventional drilling techniques.

Some research groups have developed methods that can offer limited control over solid-state nanopore size. For instance, it has been observed that by altering the beam parameters used in the drilling process, the nanopore can have a geometry such that it will either grow or shrink upon immersion in solution, depending on the original spot size of the electron beam.[44] It was also shown is this study that thermal oxidation of the nanopore following its removal from the TEM can reduce the size of the nanopore with a relatively high degree of precision.

Another interesting method to control the size of previously-drilled nanopores is the use the TEM beam itself. Depending on the original pore diameter and the membrane thickness, nanopores would either shrink or enlarge through a surface-tension-driven deformation process to minimize surface energy when softened in an electron beam.[45] Similarly, a scanning electron microscope can be used to shrink an existing nanopore by subjecting the pore to appropriate accelerating voltages.[46] Through the deposition and flow of carbonaceous materials inside the nanopore, the nanopore diameter can be accurately reduced to most desired diameters.

Despite their success at achieving nanometer control in an electron microscope, such techniques are not ideal. Firstly, these methods suffer from many of the drawbacks of conventional TEM drilling – they require the use of elaborate equipment such as a TEM or SEM, which require a skilled user, a large amount of time at very high expense. Furthermore, such equipment is very rarely located on-site, often requiring the transportation

of sample to another building or even institution, where electron microscopy resources must be shared.

Most importantly, such techniques for fine-tuning nanopore size are ultimately unreliable, as the size is determined from electron microscopy images. This can differ from the actual size of nanopore immersed in solution. As virtually all biomolecular experiments are performed in an aqueous environment, accurate knowledge of nanopore shape and geometry under experimental conditions is essential. As it has been shown that immersion in aqueous solutions can cause a nanopore to enlarge or shrink,[47] determination of the actual nanopore size during an experiment following harsh chemical treatment, plasma cleaning and rinsing stages is not possible from electron microscopy.

Considering the time and cost expense, as well as the lack of reproducibility in controlling nanopores size with TEM approaches, a rapid, inexpensive method of tuning the diameter of solid-state nanopores *in situ* (i.e. under experimental conditions) is necessary for progressing solid-sate nanopore research.

2.3.3 Solid-state nanopore noise

While both solid-state and biological nanopores are limited in their sensitivity and reliability as sensing platforms by the transient nature of the electrical signals characterizing single-molecule events, solid-state nanopores are particularly vulnerable to this limitation due to the shorter duration of events and significantly larger noise levels than protein nanopores.[22] This is especially problematic for the detection of small molecules such as proteins in medical diagnostic applications, as blockade signals are generally difficult to detect to due to the increased signal noise at the high bandwidths required to detect such short-lived events. The advantages of solid-state nanopores, however, have led to a large

breadth of investigations into understanding the various sources of noise inherent in this sensing platform,[22,48,49] as well as improving signal generation and temporal resolution to increase the amount of information that can be extracted from rapid events.[7]

The predominant sources of noise in a typical solid-state nanopore setup are associated with so-called flicker noise at low frequencies (< 1 kHz), and capacitive and dielectric loss at high frequencies.[22] Figure 2.6 illustrates a generic power spectral density plot (PSD) of current noise as a function of frequency, highlighting the dominant sources of noise with their associated frequency dependence.[15] In general, the total current power spectral density S can be represented by a polynomial of the form of equation 2-5, where f is the frequency and the terms a_0, a_1, a_2 and a_3 are contributions of flicker, thermal, dielectric and capacitive noises, respectively (discussed below).[50]

$$S(f) = \frac{a_0}{f} + a_1 + a_2 f + a_3 f^2 \qquad 2\text{-}5$$

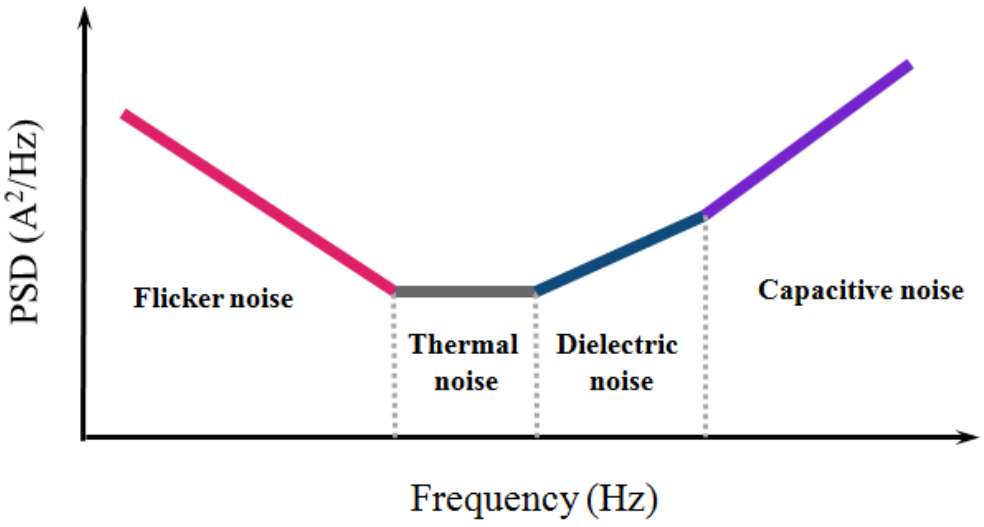

Figure 2.6 Depiction of the dominant sources of noise in the current power spectral density as a function of frequency. Flicker, thermal (shot), dielectric and capacitive contributions are shown as pink, gray, blue and purple, respectively.

Very high frequency noise (>10 kHz) is dominated by the pairing of the sum of the varying capacitances of the system and voltage noise at the input of the amplifier headstage (discussed in the following section) and is not examined in detail here. However, dielectric noise up to ~10 kHz arises from the capacitance and dielectric loss of the materials making up the nanopore membrane and support chip itself. The PSD of dielectric noise can be expressed by equation 2-6, where $kT = 4.11 \times 10^{-21}$ J at room temperature, D is the dielectric loss, and C_{chip} the capacitance of the dielectric materials composing the membrane and support structure.

$$S_{\text{dielectric}}(f) = 8\pi kTDC_{\text{chip}}f \qquad 2\text{-}6$$

In order to better understand the origin of C_{chip}, it is helpful to represent the solid-state nanopore chip with a simplified equivalent circuit diagram,[51] as shown in figure 2.7. Here, the electrical access resistance from the electrodes to the membrane, $R_{\text{electrolyte}}$, is partially dependent on the design of the fluidic cell used, but it is typically negligible for highly conductive electrolyte solutions. The R_{pore} term is the resistance of the nanopore itself, which typically includes the effects from its access resistance and wall surface charge density in most nanopore conductance calculations.[52] While usually considered insulating, the nanopore chip itself (including both the dielectric membrane and supporting doped silicon substrate) can present an electrical pathway and is denoted by $R_{\text{substrate}}$. The capacitance of the silicon nitride membrane is given by C_{membrane} and C_{sub} is the capacitance of the substrate. The latter, while comprised of the membrane capacitance in series with the capacitance of the silicon depletion layer at the silicon-electrolyte interface as well as the capacitance of the electrostatic double layer in solution, is dominated by the smallest capacitance in the path (typically either the capacitance of the silicon nitride layer or the

silicon depletion layer). The equivalent capacitance of the chip, C_{chip}, is therefore given by equation 2-7,

$$C_{\text{chip}} = \sum_i \epsilon_0 \epsilon_{r_i} A_i / t_i \qquad 2\text{-}7$$

where ϵ_0 is the permittivity of free space, ϵ_{r_i} is the relative permittivity of the dielectric layers forming the silicon nitride membrane and silicon substrate, each of thickness t_i, and A_i is the electrolyte-dielectric contact area.[15]

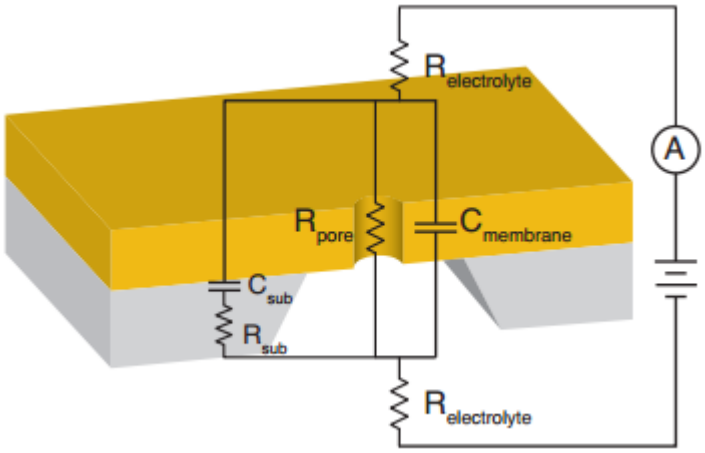

Figure 2.7 Equivalent circuit diagram superimposed on a schematic of a nanopore chip representative of those used in this thesis.

The silicon nitride membrane in which the nanopore is created acts as a non-ideal dielectric material, dissipating some electrical energy as heat which manifests as additional noise that interferes with electrical measurements. From equation 2-7, we can see that in order to improve dielectric noise properties of solid-state nanopores, the capacitance of the nanopore chip must be minimized. While not trivial, some research groups have been able to accomplish this fairly successfully by coating the surface of the nanopore chip with additional insulating layers such as polyimide[51] or PDMS[22].

In the low-frequency portion of the noise spectrum, thermal noise of the feedback resistor of the amplifier headstage and the resistance of the nanopore set a baseline limit on

signal noise in the absence of an applied potential bias.[53] This source of noise is dominated by thermal fluctuations of electrolyte ions within the pore itself and is a function of the resistance of the nanopore. Applying a potential difference across a nanopore, however, gives rise to flicker noise. Especially prevalent in solid-state nanopores, this source of noise largely dominates thermal noise at low frequencies.[22]

This low-frequency noise is a ubiquitous phenomenon that varies with the inverse of the frequency as $1/f^{\alpha}$, and is thus termed 1/f noise. It is thought that 1/f noise arises from fluctuations in the number of ions present in the nanopore, in accordance with Hooge's phenomelogical relation, and is proportional to the square of the current passing through the pore.[54] In solid-state nanopore current measurements, 1/f noise can vary by up to three orders of magnitude from pore to pore and significantly degrades electrical signals. In the initial stages of the research presented here, this source of noise was common to ~4 in 5 nanopores, making them virtually unusable for experiment.

This 1/f noise behavior is a result of various underlying mechanisms. Practically speaking, however, nanopores exhibiting excessively 1/f noise are those which have failed to completely wet and contain nano-scale bubbles.[55] As a result, such nanopores typically exhibit lower than expected conductance values than would be expected from geometrical parameters obtained from electron microscopy images, as the entire pore is no longer conductive. While it has been shown that certain cleaning procedures such as oxygen plasma or treatment with harsh chemicals can render nanopore surfaces more hydrophilic to aid wetting,[22] they are often insufficient measures and a large proportion of nanopores remain only partially wetted.

Alternatively, over the course of an experiment, molecules can adsorb to the nanopore wall, resulting in a partial clog.[24,56] Such blockages are often permanent, and attempts to remove the obstruction involve unmounting the cell and retreating with harsh chemicals or oxygen plasma. Such procedures are time consuming, risk damage to the membrane through excessive handling and are ultimately often unsuccessful in regaining low-noise characteristics. While approaches such as functionalization of the nanopore wall[26,57] have been attempted for preventing non-specific adsorption of analyte molecules, the addition of organic molecules both involve addition preparation steps and may be undesirable for certain applications. As a result, the experimental lifetime of solid-state nanopores is severely reduced, often lasting from only seconds to minutes.

As these sources of noise significantly complicate signal analysis, nanopores exhibiting high 1/f noise are typically discarded when standard cleaning procedures fail to produce clean signals.[49] As such, the actual yield of nanopores that are usable for experiment can be as low as 20%, significantly increasing the time and cost associated with solid-state nanopore production. Thus, a rapid, inexpensive way of completely wetting and rejuvenating nanopores after experiment is required for achieving acceptable fabrication yields and realizing the goal of detecting biomolecular complexes.

3 EXPERIMENTAL SETUP

3.1 Nanopore cell and housing

In a typical nanopore experiment, the nanopore serves as the only conduit for ionic current between two reservoirs of electrolytic solution. One of the attractive features of this sensing platform is its ability to transform the activity of individual molecules into a purely electrical signal. In a typical biomolecular recognition experiment, this involves the detection of picoampere changes in ionic current as biomolecules such as DNA or proteins pass through a nanopore. As such, minimization of electric noise is crucial in order to extract information about the target analyte.

In order to achieve such sensitivity, a well-shielded, low noise setup was designed. The measurement apparatus used consisted of an electrochemical cell with two polytetrafluoroethylene (PTFE) half-cells containing electrolyte chambers separated only by a nanopore, as shown in figure 3.1.[22] PTFE was used as the cell material as it is chemically inert and resistant, permitting thorough cleaning and decontamination between experiments. It is also electrically insulating so as to not interfere with electrical measurements. A key feature of the cell is its ability to form a very tight seal around the nanopore chip, with the nanopore as the only path for ionic current to flow between electrolyte reservoirs. This seal is maintained by silicone elastomer gaskets whereby the two halves of the fluidic cell compress the gaskets and nanopore chip (containing a TEM-drilled nanopore) assembly, forming a gigaohm seal between the two liquid reservoirs. Gaskets are hand-punched with an inner radius of ~1 mm to minimize contact with electrolyte solution, reducing the capacitance of the membrane, while ensuring exposure of the nanopore to each electrolyte reservoir.

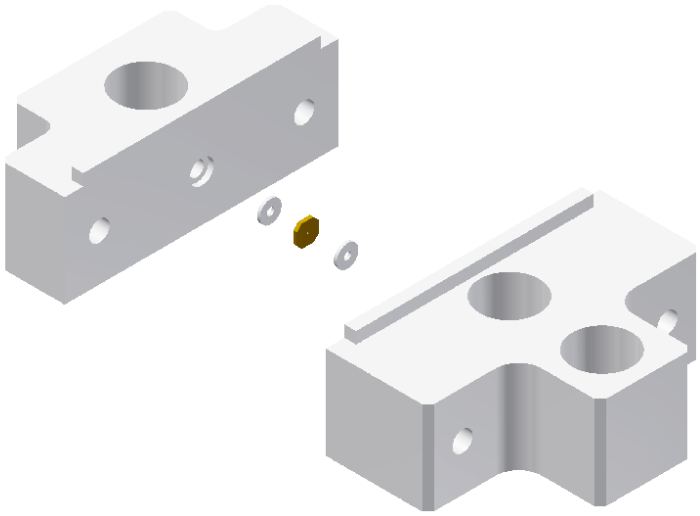

Figure 3.1 Exploded view of the electrochemical cell assembly. The silicon nitride nanopore chip is sandwiched between silicone elastomer gaskets, which are in turn compressed by the two half-cells, creating a gigaohm seal between reservoirs.

The two reservoirs were filled with 1-2 M KCl or LiCl electrolyte solution buffered at pH 8.0. The ionic species and concentration were varied depending on the application. Unless otherwise specified, 1 M KCl was used for characterizing nanopore conductivity and noise spectra, while 2 M KCl was typically used for detecting DNA translocation. In attempts to slow translocation events for the detection of DNA-protein complexes in section 6, 1 M LiCl was used. While no experiments were performed with temperature control, the third well in the electrolytic cell could be used to calibrate the temperature of the cell using a thermistor, or filled with H_2O when the cell was sealed to prevent evaporation of electrolyte.

Ag/AgCl electrodes submerged in each reservoir were used to apply potential biases and measure the resultant ionic current. Ag/AgCl electrodes were used as they do not contribute a significant amount of noise to the ionic current signal and are considered non-polarizable, reversible electrodes. These were created by soldering Ag wire to a gold-plated contact pin at one end and subsequent encapsulation by PTFE heat-shrinkable tubing with one end exposed. The exposed electrode was cleaned in concentrated HNO_3 for 3 min,

thoroughly rinsed and immersed in concentrated bleach for 1 hr to plate with Cl. Electrodes were routinely cleaned using the same procedure with 10% HNO_3.

In order to shield the electrodes and nanopore from external noise, the electrochemical cell was placed inside a grounded primary Faraday cage. This consisted of an aluminum block machined to the specifications shown in Appendix I. The block consisted of a pit in which the cell could be inserted and completely covered with an aluminum lid with small slits to allow for insertion of the electrodes, which are clamped down by an aluminum plate. While temperature control was not used in the experiments discussed in this thesis, the aluminum block contained a U-shaped channel in which fittings and tubing could be inserted to allow for externally heated/cooled water to be passed through, regulating temperature. While rapid changes in temperature would not be possible with such a setup, stable temperatures could be achieved without introducing additional electric noise that would be produced by thermoelectric modules. An image of the primary Faraday shield containing the nanopore cell and electrodes can be seen in figure 3.2, without the conductive metal lid.

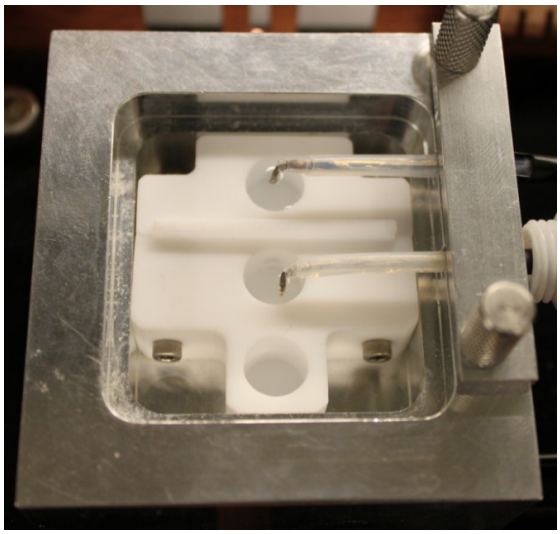

Figure 3.2 Nanopore cell and primary Faraday cage. The aluminum block provides a shield to external electrical noise and allows for externally temperature-controlled water to be passed through, cooling the nanopore cell. A plate is screwed into the block to clamp the electrodes in place, while an aluminum cover (not shown) completes the Faraday cage. The block is thermally isolated from the secondary Faraday cage by an acrylic plate.

Ultra low-noise current measurements are acquired using an Axopatch 200B patch clamp amplifier. In order to minimize external electrical noise, the electrodes from the cell are connected to the amplifier headstage inside of a grounded secondary Faraday cage. This secondary cage, machined as per the specifications shown in Appendix I, was made of copper and was large enough to accommodate the amplifier headstage and aluminum block housing the nanopore cell, from which it was thermally insulated with an acrylic base in order to reduce the amount of metal to be cooled in the case of a temperature-controlled experiment. This acrylic base also provides a base on which the aluminum block and headstage can be fixed. In order to minimize the amount of exposed electrode wiring, the base is cut such that when connected, there is no separation between the block and headstage. Additionally, the copper box was machined to allow access of tubing containing temperature-controlled water and wiring for electrical measurement and temperature sensing.

Mechanical vibrations are minimized by placing the copper box on 1 cm thick elastomer pads. An image of the apparatus is shown in figure 3.3.

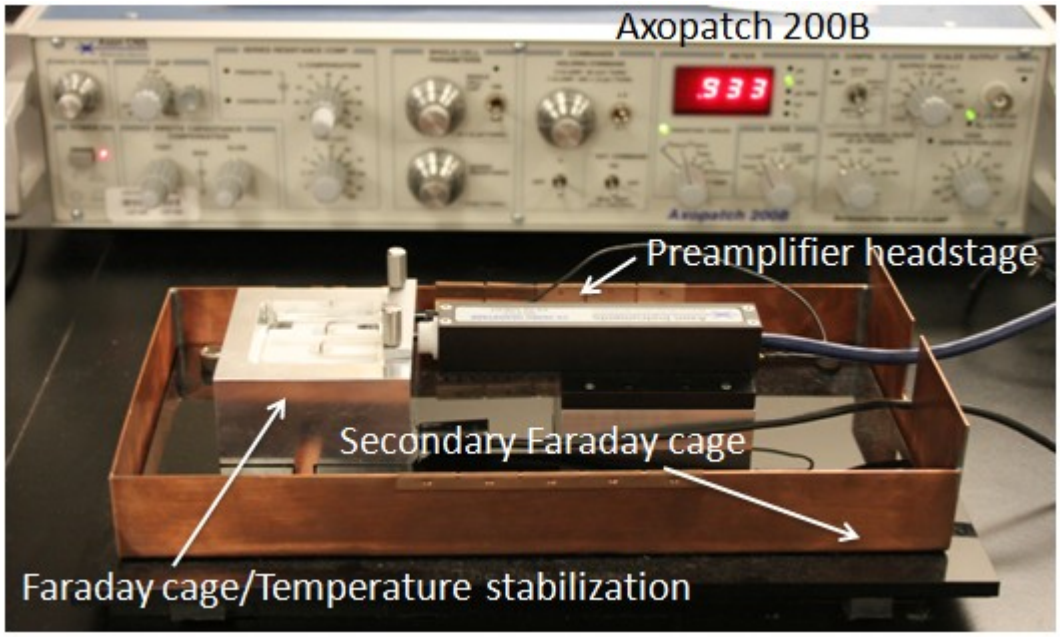

Figure 3.3 Image of the low-noise nanopore apparatus. The nanopore cell is shielded by a primary Faraday cage, which is in turn enclosed with the Axopatch headstage inside a secondary Faraday cage to minimize external noise.

The electrical signals are amplified by the headstage and connected through openings in the secondary Faraday cage to the Axopatch console. This component provides a voltage source for biases up to 1 V and measures current with picoampere sensitivity up to 200 nA. Analogue signals from the amplifier are digitized with a National Instruments data acquisition (DAQ) card (PCIe-6351) connected to a computer and can also be sent directly to an oscilloscope for real-time monitoring. The DAQ card is also used to control the amplifier's sourced voltage and record ionic current readings using custom-written Labview software. A schematic of the recording setup can is shown in figure 3.4.

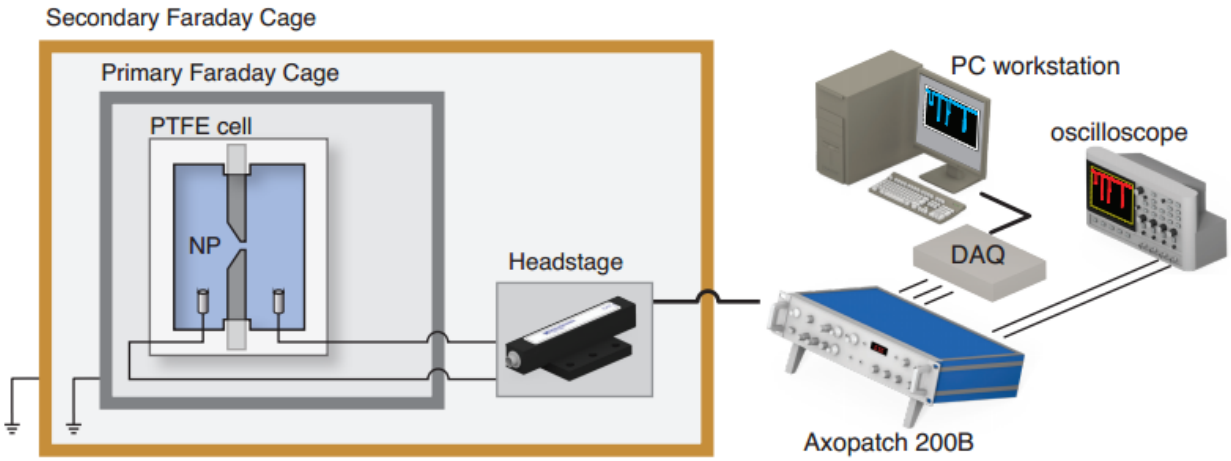

Figure 3.4 Schematic diagram of the nanopore electrical setup. The headstage is connected to the Axopatch, which serves as a voltage source and current measurement device and is computer-controlled via a data acquisition card. Electrical measurements are viewed in real time using an oscilloscope.

3.2 Cleaning and mounting a nanopore

The most crucial aspect of a successful solid-state nanopore experiment is proper preparation of the nanopore chip. This involves careful handling, cleaning and mounting of the nanopore chip in the electrochemical cell. As exposure to the electron beam during drilling and subsequent contact with air can lead to oxidation and/or carbon deposition on the nanopore surface, rigorous cleaning is necessary to remove any hydrophobic residues and render the pore hydrophilic to allow for complete wetting.[22] While oxygen plasma has been shown to be successful at doing this,[49] it was found that nanopores treated with oxygen plasma in the lab were unstable and were liable to grow uncontrollably once immersed in electrolyte solution. Thus, while loosely based on existing procedures, the following protocol was established in order to reliably prepare a nanopore for experiment.

1. Clean the nanopore cell by placing in a beaker of 20% HNO_3 and boiling for 10 min to remove any residual DNA contamination from previous experiments. Rinse with copious

amounts of filtered H_2O and dry under compressed air. Store in a clean, dust-free environment until use.

2. Preset hot plate to 85°C in a fume hood.

3. Prepare piranha cleaning solution by pipetting 3 mL of concentrated H_2SO_4 followed by 1 mL of H_2O_2 into a 10 mL beaker. Gently reflux to ensure proper mixing of the solution, which will rapidly heat up and may begin to boil.

4. Using acid-resistant tweezers, place a nanopore chip in the piranha solution. To prevent floating and ensure that complete immersion, insert edge first until it is completely submerged. Piranha solution is extremely reactive and will remove any organic compounds on the surface of the membrane and will render the nanopore hydrophilic. This will aid in wetting the nanopore as discussed in section 2.3.

5. Rinse tweezers with copious amounts of water to remove any trace piranha solution.

6. Place the beaker containing the nanopore chip on the preheated hot plate for 30-45 min. Periodically check to ensure that the nanopore chip remains submerged, as bubbles can form on its surface and cause it to float and prevent piranha solution from coming into contact with the entire membrane surface.

7. While the nanopore chip is being cleaned, degas ~50 mL of filtered H_2O and buffered salt solution. This can be done by sonicating in a heated water bath at 35°C followed by placement in a vacuum chamber for 30 min. Mildly heating the water reduces its capacity to dissolve gases can and will help in the degassing process.

Additionally, clean two silicone elastomer gaskets by placing in a small beaker containing 1:1 mixture of EtOH:H_2O and sonicating for 15 min. When clean, remove the gaskets from the solution, suction dry using an aspirator and place on a clean glass slide.

8. Remove the beaker containing the nanopore chip from the hot plate. Being careful not to damage the membrane, remove piranha solution from the beaker using a pipette and discard in a waste beaker containing 1 L H_2O.

9. Rinse the beaker and nanopore chip with ~5 mL degassed filtered H_2O. Gently reflux and remove H_2O. Repeat 4-5 times. This will ensure that all piranha solution is removed from the beaker.

10. Remove H_2O from the beaker and replace with ethanol. Ethanol evaporates more readily than water and will leave a cleaner membrane surface when dried.

11. Remove ethanol from the beaker. Using clean sharp-tip tweezers, gently grip the edge of the nanopore chip and remove it from the beaker.

12. Carefully dry the chip by applying suction to its edge using an aspirator. Rapidly removing ethanol in this fashion minimized the deposition of contaminants on the membrane surface. When dry, place the chip on a clean gasket such that the membrane window is aligned with the gasket opening.

13. Place the second gasket above the nanopore chip, again aligning the membrane window with the gasket opening. Inspect the chip under the microscope at 10X magnification under a stereomicroscope equipped with coaxial episcopic illumination to verify membrane integrity and ensure proper alignment of the gaskets. If the membrane window is not centered in the gasket openings, carefully remove the gaskets and realign.

14. Place chip and gasket assembly into one half of the PTFE cell and carefully align the second half above the first. Seal by firmly screwing the two half-cells together. (Refer to figure 3.1)

15. To wet the pore, flush both the *cis* and *trans* reservoirs with ethanol and place the cell in a vacuum chamber. This will remove any trapped air pockets in the small channels leading to the nanopore chip.

16. Remove ethanol by flushing both reservoirs with 5 mL of degassed, buffered salt solution with a syringe, drawing away overflow with an aspirator. Repeat this 2-3 times to completely remove alcohol.

Following these steps, the nanopore cell is ready for characterization. It can then be placed in the primary Faraday cage and the electrodes clamped into place and connected to the patch clamp amplifier headstage for characterization, which is described in the following sections.

3.3 Nanopore size characterization

In order to extract information from electrical signals in a biomolecular experiment, the size of a nanopore must first be known. It is crucial that the actual size of the nanopore under experimental conditions be measured, as this can often differ from that determined by electron microscopy following harsh chemical treatment and immersion in aqueous solutions.[47]

The quantification of nanopore size begins with a measurement of the nanopore conductance. If the general 3D shape of the nanopore is known, the conductance can be used to infer its diameter.[52,58,59] It has been shown using TEM tomography that solid-state nanopores drilled using a TEM have a double-cone, or hourglass geometry (neglecting subsequent shrinking/enlarging and surface reorganization).[59] However, nanopore

dimensions can be well approximated from measurements of conductance assuming a cylindrical geometry with an effective length, as shown in figure 3.5.

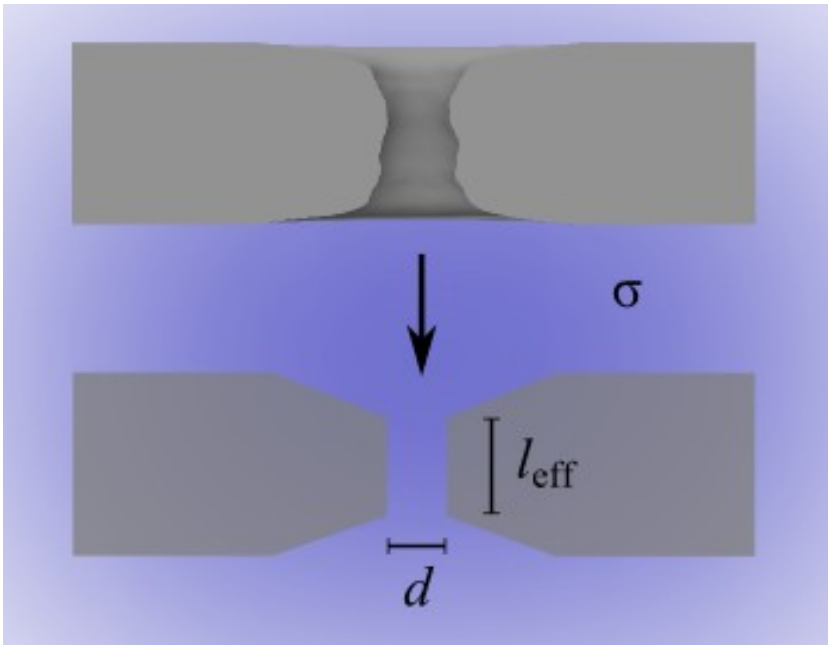

Figure 3.5 Schematic of solid-state nanopore geometry. The conductance of the nanopore in a solution of conductivity σ can be used to infer its diameter d assuming a cylindrical pore of effective length l_{eff}, typically ~1/2 the membrane thickness.

While various relationships between the diameter of a solid-state nanopore and its conductance G in solution have been developed, the one proposed by Kowalczyk, *et al.*[52] shows excellent agreement between theory and experimental values. Shown in equation 3-1, the nanopore diameter d can be calculated by assuming a cylindrical geometry with an effective length l_{eff}, which is typically half of the membrane thickness. For the nanopores studied here, l_{eff} = 15 nm, and the conductivity of the electrolyte solution σ = 11.3 Sm^{-1} for 1 M KCl. In equation 3-1, the first term is associated with the resistance of the nanopore itself while the second term accounts for access resistance (the resistance of the electrolyte solution in a narrow region around, but not inside of the nanopore). While the latter term

can be almost negligible for small pores, it becomes increasingly significant for nanopores >15 nm in diameter.

$$G = \sigma \left[\frac{4l_{\text{eff}}}{\pi d^2} + \frac{1}{d}\right]^{-1} \qquad 3\text{-}1$$

The conductance or inverse of resistance of a nanopore can be determined from Ohm's law from the current-voltage (IV) characteristics of the nanopore. Below +/- 1 V, the IV characteristics of silicon nitride nanopores drilled using a TEM are linear and behave as ideal ohmic resistors. Thus, nanopore conductance is calculated by fitting a linear IV curve. As shown in figure 3.5, this was done by recording the level of ionic current through the pore as the applied potential was swept from -200 mV to +200 mV in steps of 20 mV. In these measurements, current values are acquired at a sampling frequency of 10 kHz for 1 s at each interval. For the nanopore shown in figure 3.6, the IV characteristics of a 7 nm pore (as determined by TEM imaging) in 1 M KCl at pH 8.0 gives a conductance of 8.9 nS, corresponding to a calculated diameter of 4.3 nm. This discrepancy in diameter measurements between the TEM image and that calculated from nanopore conductance highlights the importance of characterizing the nanopore size in experimental conditions, as harsh chemical cleaning and subsequent immersion in aqueous solutions can have a great effect on the final nanopore geometry.

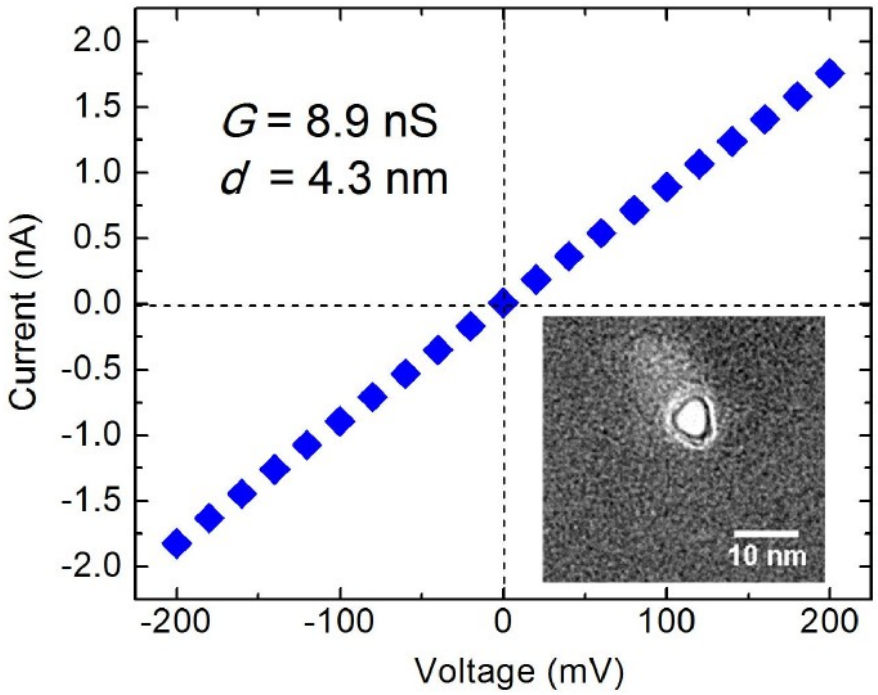

Figure 3.6 IV characteristics of a 4.3 nm diameter nanopore over an applied voltage range of +/- 200 mV. A TEM image of the nanopore is shown in the inset.

If the conductance is significantly lower than expected or strong asymmetry is present in the IV curve, the nanopore is likely not completely wet and contains nanobubbles[55] or other contaminating debris. Conversely, if the conductance is too high, there is likely a leak in the nanopore-gasket assembly. Relatively small deviations from the expected conductance value can be due to variability in effective pore length or alteration of nanopore geometry following harsh chemical treatment and immersion in aqueous solution.

3.4 Electrical noise characterization

As discussed in section 2.3.3, a significant challenge associated with solid-state nanopore sensing platforms is the control of electrical noise. Various noise sources can drastically reduce signal quality and interfere with the detection and characterization of analyte molecules. While care can be taken to minimize external electromagnetic interference with

proper shielding as detailed in the previous sections, pore-to-pore variability in noise amplitude can be as large as three orders of magnitude. Characterization of electrical noise for each pore is thus essential for ascertaining the ability of a nanopore to perform in single molecule experiments.

Quantitative analysis of electric noise is performed using PSD plots of ionic current noise amplitude. In order to identify various sources of noise, PSD plots were obtained at constant potential biases of 0 mV and 200 mV, as shown in figure 3.7a. As transient event blockages of ionic current upon translocation of molecules can be as short-lived as tens of microseconds, ionic current measurements were acquired at 250 kHz and filtered by the Axopatch's100 kHz 4-pole Bessel filter. Noise characterization experiments were run for 30 s with and without applied voltage. The resultant PSDs were calculated using custom Labview software by averaging thirty 1 s current segments, providing easily resolvable peaks in the spectra for identification of noise sources.

From figure 3.7a, the PSD of a nanopore in the presence of an applied bias shows considerably more low-frequency noise than when no bias is applied and varies with 1/f dependence. At 0 mV, noise amplitude is small enough to resolve a small peak around 30 Hz. By adjusting the electrode clamp pressure, it was found that this peak in noise amplitude corresponds to vibration of the Ag/AgCl electrodes in the primary Faraday cage. Above ~10 kHz, the PSDs appear quite similar as the dominant sources of noise at high frequencies arise from the dielectric properties of the silicon nitride membrane and amplifier headstage. The abrupt drop off above 50 kHz in both cases is a result of the 100 kHz low-pass filter.

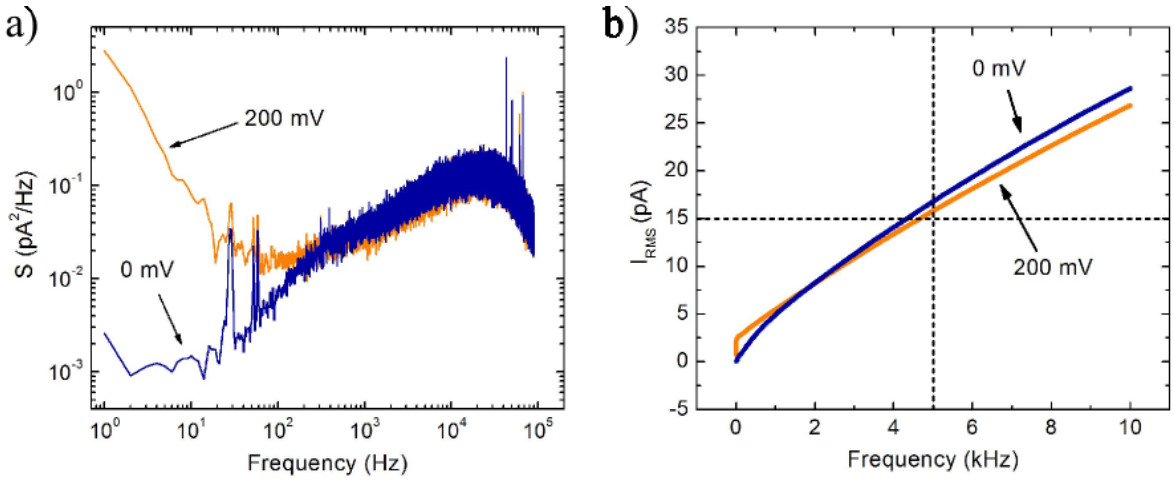

Figure 3.7 a) PSD plots of a 9 nm silicon nitride nanopore at 0 mV and 200 mV. Sources of noise can be identified by the location of peaks corresponding to large noise amplitude. b) I_{rms} noise calculated from the PSDs in (a). Analysis of the I_{rms} noise spectra can be used to determine which frequencies contribute significantly to the noise of the system.

It is often useful to express the noise amplitude in terms of root-mean-square current noise (I_{rms}).[22] This is determined by taking the square root of the integral of the power spectral density and is shown in figure 3.7b. The I_{rms} increases with the square root of the bandwidth and can be used to determine which frequencies provide significant contributions to the noise of the system. In figure 3.7b, the I_{rms} noise is larger when pores are subjected to a potential bias for frequencies < 2 kHz. Typically, the I_{rms} noise at a 5 kHz bandwidth is used to determine whether a nanopore can be considered "low-noise" and used for experiment, as discussed in section 4.2.

3.5 Application of high electric fields for *in situ* nanopore conditioning

On the road to realizing the goal of disease biomarker detection using solid-state nanopores, the fundamental challenges associated with this sensing platform, namely size control, noise reduction and improved fabrication yield and short lifetimes, must be overcome. Here we introduce a method of conditioning nanopores that is capable of

addressing these issues. As discussed in the following sections, by applying short pulses (0.1-2 s) of relatively high voltage (6-10 V), it is possible to simultaneously enlarge a nanopore with sub-nanometer precision and achieve low-noise current signals with a significantly improved fabrication yield. This technique is capable of rejuvenating used nanopores for further experiment through the removal of adsorbed debris and is performed entirely under experimental conditions using standard laboratory equipment.

The process for preparing a nanopore for a molecular recognition experiment involves the automated cyclic application of high electric field pulses produced by stepping the potential up to 6-10 V. As the potential differences required and resultant ionic currents are beyond the capabilities of the Axopatch, the computer-controlled DAQ card is used to directly output the desired voltage to one electrode. The resultant ionic current is measured by a Keithley 428 current amplifier connected in series with the other electrode and digitized by the DAQ card. The entire process is controlled and monitored by a custom-written Labview program and can be fully automated. A schematic of the setup is shown in figure 3.8.

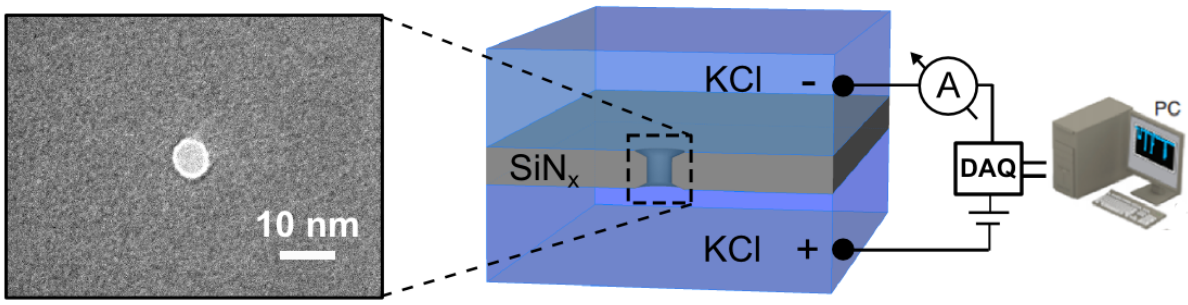

Figure 3.8 Schematic of the apparatus used to condition nanopores with high electric fields. Potentials of 6-10 V are output directly from the DAQ card and the resultant ionic current is measured with a Keithley 428 current amplifier. The entire automated process is controlled by a custom-written Labview program.

4 ENLARGING AND NOISE REDUCTION USING HIGH ELECTRIC FIELDS

4.1 Size control

Solid-state nanopore size is an important parameter not only for maximization of the signal amplitude of single-molecule events but also in dictating the range of applications for which a nanopore can be used. Applications such as the detection of DNA-protein complexes require dimensions large enough to accommodate bulky molecules without being so big as to lose sensitivity and resolution. As discussed in section 2.3, precise control over nanopore size is difficult to achieve using standard TEM drilling techniques and those created are typically limited to sub-10 nm dimensions. Application of high electric field pulses, on the other hand, offers sub-nanometer control over final nanopore size in under experimental conditions without the use of an elaborate, costly apparatus.

4.1.1 Precise control of size using high electric fields

While typical experiments are run at relatively low voltages (0.1-0.5 V), by applying a larger potential difference (6-10 V) across a nanopore, its conductance can be precisely tuned through an enlargement process in which pore surface atoms are removed in a strong electric field (0.20-0.33 V/nm). By applying short, high electric field pulses, the conductance of a nanopore can be increased in small steps depending on the strength and duration of each pulse and the original size of the nanopore. Fine tuning of final nanopore conductance relies on the cyclic application of high electric field alternated with low voltage bias measurement periods of 400 mV. From equation 3-1, the diameter of the nanopore can be calculated from the measured conductance in real-time.

Figure 4.1 shows how by applying 8 V pulses of 2 s duration, the ionic current through the nanopore increases in steps of approximately 1.3 nA after each pulse,

corresponding to an increase in conductance of ΔG = 3.3 nS. The resultant increase in nanopore diameter per cycle under these conditions is ~0.4 nm. While variability in membrane thickness, surface chemistry and initial nanopore geometry yields different growth rates from pore to pore, the magnitude and duration of each high field pulse can be adjusted to precisely control the amount of growth per cycle. Due to the relatively high capacitance of the nanopore device, measurement periods at 400 mV are extended to 7 s to allow for the capacitive current to dissipate and the faradaic current to stabilize after each voltage pulse. When a desired conductance value (i.e. diameter) is detected by the controlling Labview software, the automated process is simply stopped.

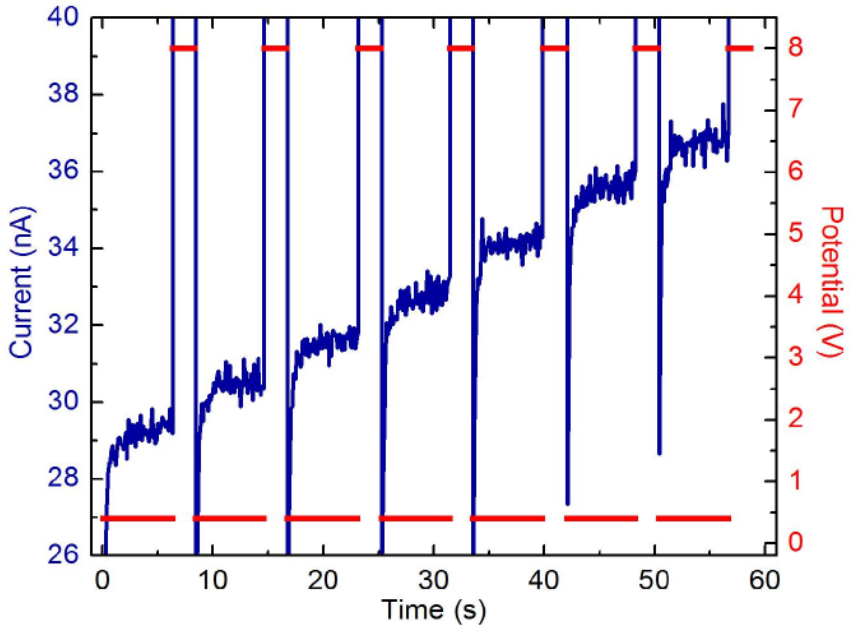

Figure 4.1 Increasing ionic current (blue) upon treatment with high voltage pulses in 1 M KCl. Voltage (red) is alternated between 2 s pulses of 8 V and measurement periods 7 s at 400 mV. Current is sampled at 1 kHz and averaged every hundred points for display.

In figure 4.1, current values during high electric field pulses are not shown, as the current measured during pulses is not a true indication of the nanopore conductance. This is because at high potentials, the 30 nm thick SiN membrane appears to exhibit leakage current

at high potentials. This is shown in figure 4.2, where a blank membrane (not containing a nanopore) is seen to exhibit conductance for voltage pulses >4 V. Thus, a measurement period is necessary to accurately measure the increase in nanopore conductance during growth.

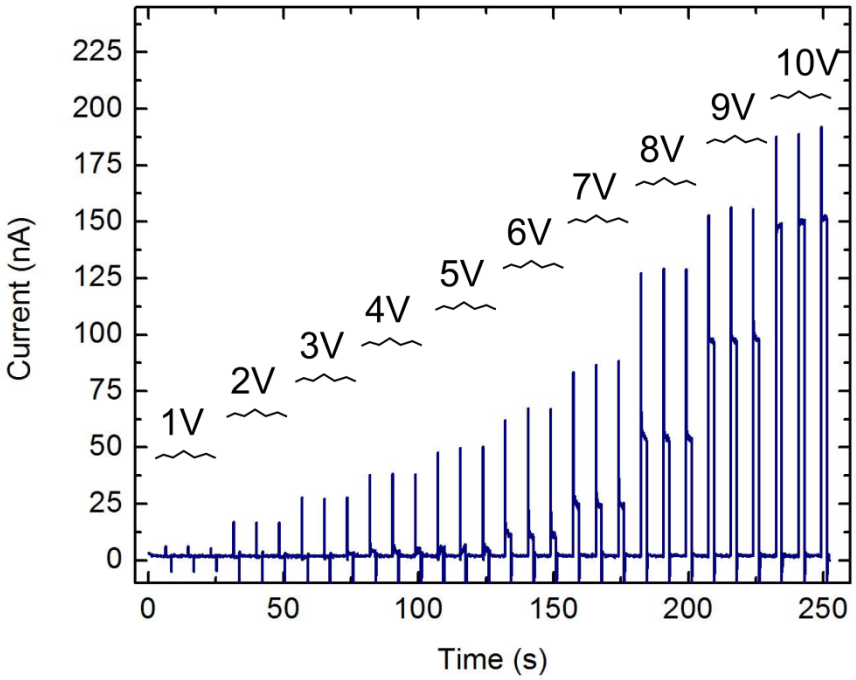

Figure 4.2 Current measured across a blank membrane for alternating measurement potentials of 400 mV and pulse biases incrementing from 1-10 V. For potentials >4 V, the blank membrane exhibits non-zero conductance illustrating the difficulty in calculating pore diameter at high biases.

The range of final nanopore sizes is limited only by the initial diameter of the nanopore, as the process can simply be continued until the desired conductance level is measured. Figure 4.3a shows the IV characteristics of several examples of nanopores enlarged to various diameters. In the sub-1V voltage bias range, enlarged pores act as ideal ohmic resistors with linear IV curves, a trend that is consistent over multiple enlarged nanopores (N = 20). Of note is the fact that conductance values are constant even after

unmounting a nanopore and flushing the system with fresh electrolyte solution, indicating that the observed increase in conductance is not a transient effect caused by local heating of the electrolyte in the nanopore, for example. Moreover, the conductance of nanopores treated with high field pulses is stable up to several days after treatment. This is shown in figure 4.3b where the conductance of two nanopores enlarged to 68 nS and 111 nS were determined on a daily basis by IV curve analysis. Prior to each measurement, the nanopores were flushed with fresh 1 M KCl at pH 8.0.

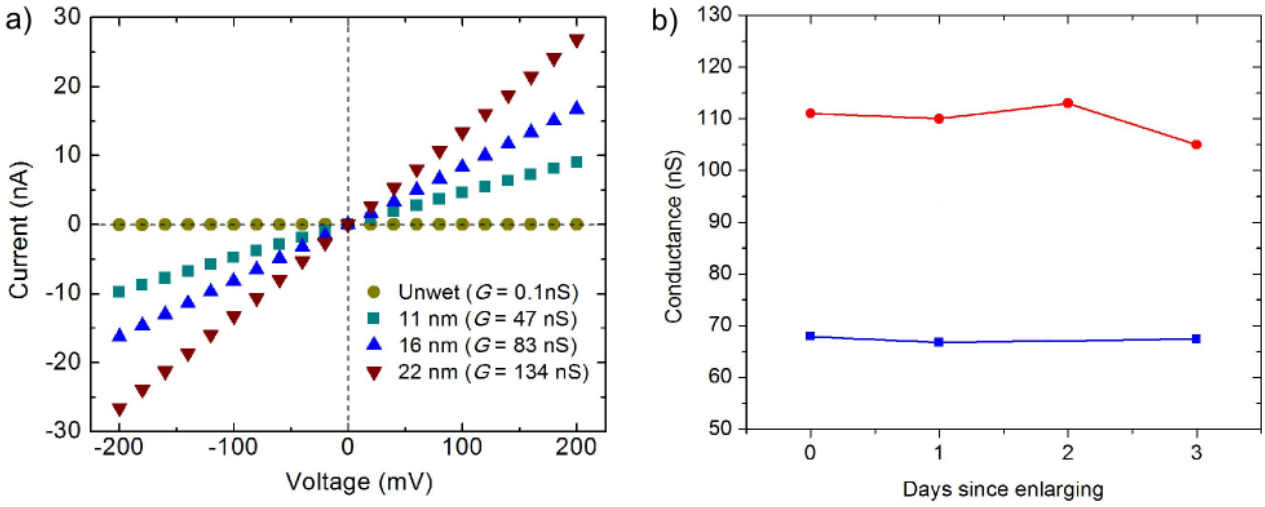

Figure 4.3 (a) IV characteristics of various enlarged pores 30 min after enlarging. The yellow curve is data from an untreated pore that did not wet, and thus had almost no conductance. Upon high field pulses, the pore wetted and was enlarged to 22 nm (red). Green and blue curves were pores enlarged to 11 nm and 16 nm, respectively. In the voltage range of ±200 mV, the pores have a constant conductance which was used to calculate pore diameter. (b) Conductance values of two enlarged nanopores following flushing with fresh 1 M KCl solution as a function of the amount of days since enlargement. Day 0 corresponds to the conductance immediately after enlarging and flushing with new solution.

Ideally, TEM images could be obtained to visually confirm the sizing data following treatment with high electric fields presented. However, in practice it is extremely difficult to locate nanopores once they have been removed from the TEM following initial drilling. While many attempts were made to visualize enlarged pores, the challenge of locating a 10-

30 nm diameter pore on a 50x50 μm membrane containing thousands of residual salt deposits following immersion and exposure to experimental conditions proved too difficult. However, as discussed in section 5.2, analysis of DNA translocation data provide strong evidence supporting the measured increase in conductance as being a result of an enlarging process.

4.1.2 Varying growth rate

In order to further understand the enlargement process, the dependence of nanopore growth on the electric field strength was investigated. From figure 4.4a, varying the pulse strength from 6 to 10 V (0.20-0.33 V/nm) produces quite different growth profiles. In each case, nanopores were immersed in 1 M KCl solution and the pulse duration was kept constant at 2 s. When subjected to a 6 V potential bias, nanopore growth is relatively minor with conductance increasing by ~25 nS over 1000 s of exposure time (0.03 nSs^{-1}). In comparison, pores subjected to 8 V and 10 V increase in conductance at an average rate of ~0.10 nSs^{-1} and 0.63 nSs^{-1}, respectively. However, several different growth regimes are observed depending on the stage of enlargement and the applied bias. While nanopore growth at 6 V is approximately linear throughout most of the time window shown, it increases over time at 8 V and more drastically at 10 V. Additionally, nanopore growth appears to initially slow for the first 200 s of exposure to 6 V and 8 V, as highlighted in figure 4.4b. For the 10 V case, this initial growth is characterized by a sharp increase in conductance from 10 nS to 14 nS after ~85 s. From noise characteristics of the nanopore before and after enlarging, this jump in conductance is attributed to complete wetting of the nanopore, as discussed in section 4.2.

When subjected to pulses larger than 6 V, nanopore growth rate increases throughout the enlarging process; that is, larger pores grow faster than smaller ones. This is illustrated in figure 4.4c, where the growth rate of the nanopores subjected to 8 V and 10 V increases as a function of the conductance measured before each high electric field pulse. For the 10 V case, growth rate is plotted from data acquired after the initial 100 s of enlarging, following complete wetting of the nanopore. We find that in the conductance window shown, nanopore growth rate is approximately parabolic, ranging between 0.01-0.40 nSs^{-1} and 0.01-11 nSs^{-1} for 8 V and 10 V applied biases, respectively. Interestingly, this increase in conductance corresponds to a growth rate of less than 0.1 nm per second, assuming a cylindrical nanopore with an effective length of 15 nm. This method is thus very powerful for obtaining precise control over final nanopore size. It should also be noted that for nanopores of conductance greater than 150 nS, growth is less predictable for biases of 8-10 V, although pulse strength can be tuned to offer better control.

While it is clear from the different growth rates of the nanopores shown in figure 4.4 that the strength of the electric field plays a significant role in the enlarging of nanopores, a complete understanding of the growth process is not yet clear. In fact, several mechanisms are likely involved in the growth process. The initial slowdown in the increase of the growth rate (figure 4.4b), which seems common to many nanopores investigated, could be related to the initial modification of the nanopore profile or to the removal of weakly bound residual carbonaceous contamination that may be left over from the TEM drilling and imaging process, as discussed in section 2.3. But as the nanopore is enlarged, the increasing growth rate for large conductance values in figure 4.4c seems to indicate a relationship between

growth rate and the amount of current passing through the nanopore, as the applied bias and pulse duration are kept constant throughout the experiment.

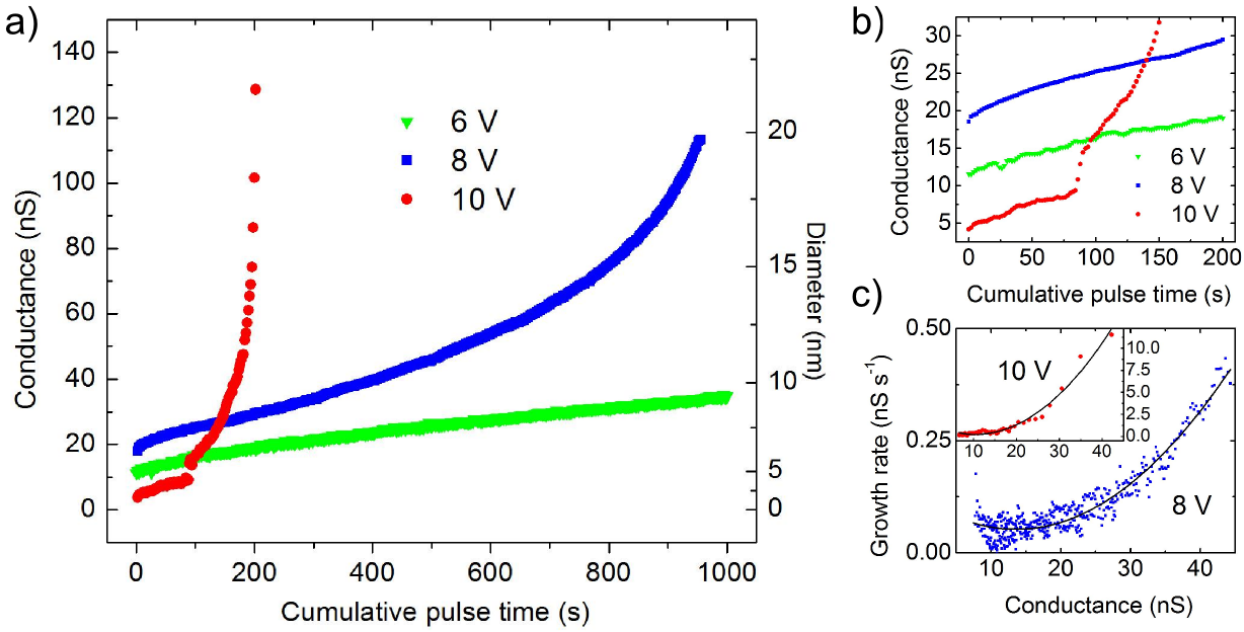

Figure 4.4 (a) Enlargement of nanopores upon 2 s pulses of 6 V (green), 8 V (blue) and 10 V (red) in 1 M KCl. After each pulse, current measurements were acquired at 400 mV at 1 kHz for 7 s. After 2 s of measurement, current values over the next 5 s were averaged and used to calculate the conductance of the nanopore, shown as a function of the cumulative pulse time of the experiment. (b) An enlarged view of the first 200 s of nanopore growth showing a decrease in growth rate with time. At 10 V, complete wetting of the nanopore is seen as a sharp increase in conductance after 85 s. (c) Growth rate of as a function of nanopore conductance prior to each 8 V (blue) and 10 V (red) pulse appears approximately parabolic (fits to 2nd degree polynomials shown as solid black lines). Only conductance values for 10 V pulses following complete wetting are shown.

Pore-to-pore variability in growth rate under identical experimental conditions, such as in figure 4.5, makes elucidation of a complete mechanism difficult. In this case, both nanopores were enlarged with 8 V pulses of 2s duration in 1 M KCl. Clearly growth rates can vary significantly, even for a given nanopore size. It should be noted however that the nanopore represented by the green curve was first enlarged to its initial size using 6 V pulses, which may have affected its initial growth profile.

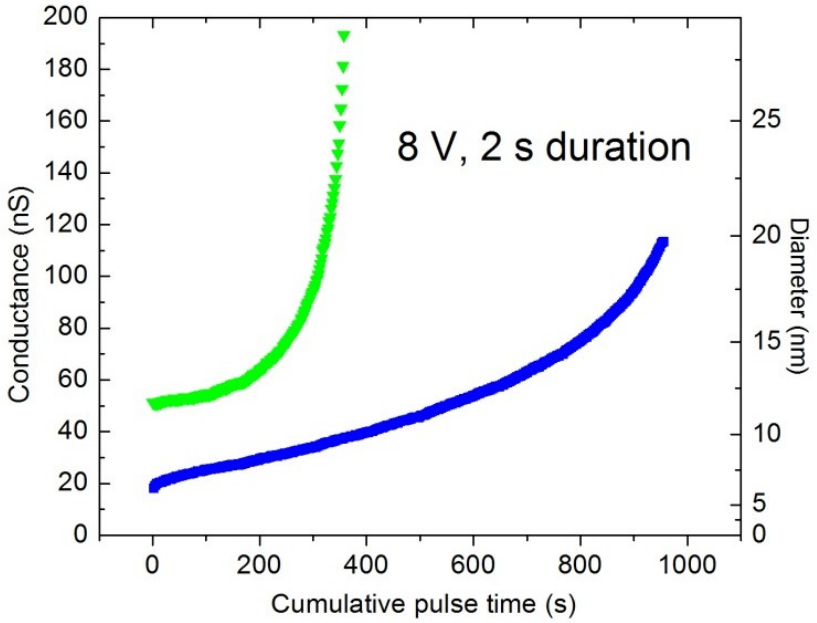

Figure 4.5 Nanopore growth upon application of 8 V pulses of 2 s duration. Diameter values are calculated assuming a cylindrical nanopore geometry assuming an effective thickness of 15 nm, as described in the text.

Figure 4.6 shows the growth profiles of all of the nanopores whose complete enlargement profiles were investigated (i.e. from first mounting to >100 nS). This includes nanopores enlarged using various pulse strengths as well as with varying ionic strength of electrolyte solution. While there appears to be some evidence of being able to accelerate nanopore enlarging by increasing the ionic strength, identifying the underlying mechanisms controlling grown remains a challenge. Preliminary data (not shown) seems to indicate that at low salt concentrations (10 mM KCl), growth is not observed at voltage below 8V, further reinforcing the notion of a relationship between the nanopore growth and amount of ionic current challenging the pore, but does not as yet provide a complete understanding of the growth process.

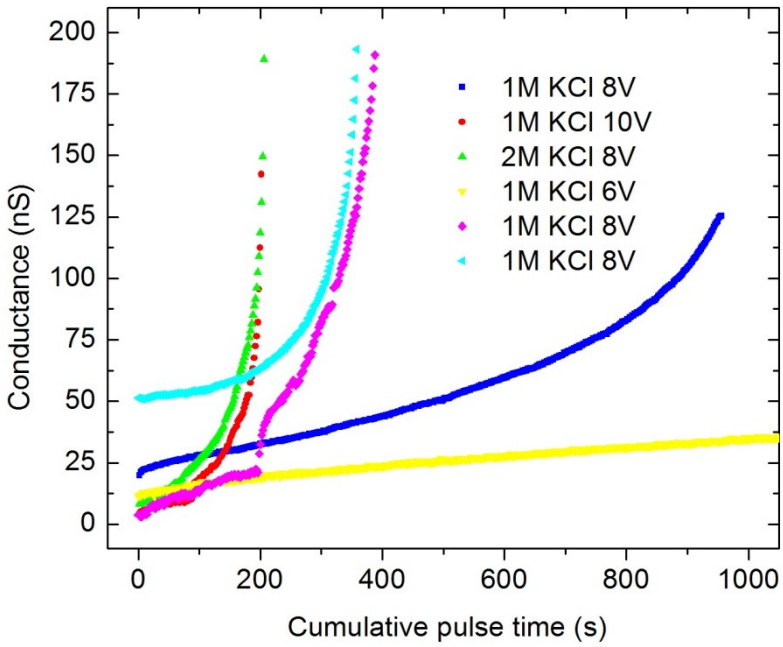

Figure 4.6 Nanopore growth upon application of 6-10 V pulses of 2 s duration. The concentration of KCl in solution was varied from 1-2 M as indicated.

Ascertaining the exact roles of power dissipation, electro-osmotic flow, resistive heating and electrochemistry occurring at the nanopore surface in the enlargement process remains a formidable challenge and is outside the scope of this thesis. From a practical standpoint, however, cyclic application of high field pulses provides a means of controlling nanopore size with exceptional precision, as the nanopore diameter can be increased in sub-nanometer steps in an automated fashion simply by varying the pulse strength and level of ionic current *in situ* under experimental conditions.

4.2 Noise reduction

In addition to providing control over pore size, application of short high electric field pulses significantly reduces low frequency noise in nanopore current measurements. As discussed in section 2.3.3, 1/f noise is thought to arise in solid-state nanopores studies when nanopores fail to completely wet [55], or when, over the course of an experiment, translocating

molecules adsorb to the nanopore wall [24,56], resulting in a partial clog. By applying short high field pulses, such pores are readily and rapidly cleaned *in situ*, without risking accidental damage to the membrane or requiring lengthy procedures associated with manipulating the nanopore membrane.

By maintaining a short pulse time (< 500 ms), it is possible to clean a nanopore while avoiding significant enlargement of the nanopore. Figure 4.7 shows the PSD plots of two nanopores for an applied bias of 200 mV both before and after the application 8-10 V pulses of 200 ms duration. As the dielectric properties of the SiN membranes and the amplifier headstage are the predominant sources of noise above 10 kHz, these portions of the PSD remain relatively unchanged from pore to pore. Below ~1 kHz, however, low frequency noise varies as $1/f^{\alpha}$ with $0.94 < \alpha < 1.5$ and can be significantly lowered upon treatment with high electric fields. For instance, the orange curve in figure 4.7 is a typical PSD of a pore that had become irreversibly clogged during a DNA translocation experiment and two separate washes in piranha solution at 75 °C for 30 min were unable to regenerate a low noise current trace. The red curve, however, shows the PSD of an 11 nm (G = 47.0 nS) clogged pore that was cleaned using 200 ms pulses of 10 V. In this example, 2 pulses were enough to remove the source of noise and leave a clean nanopore surface with a very stable conductance, illustrated by a three orders of magnitude decrease in low frequency noise below 500 Hz.

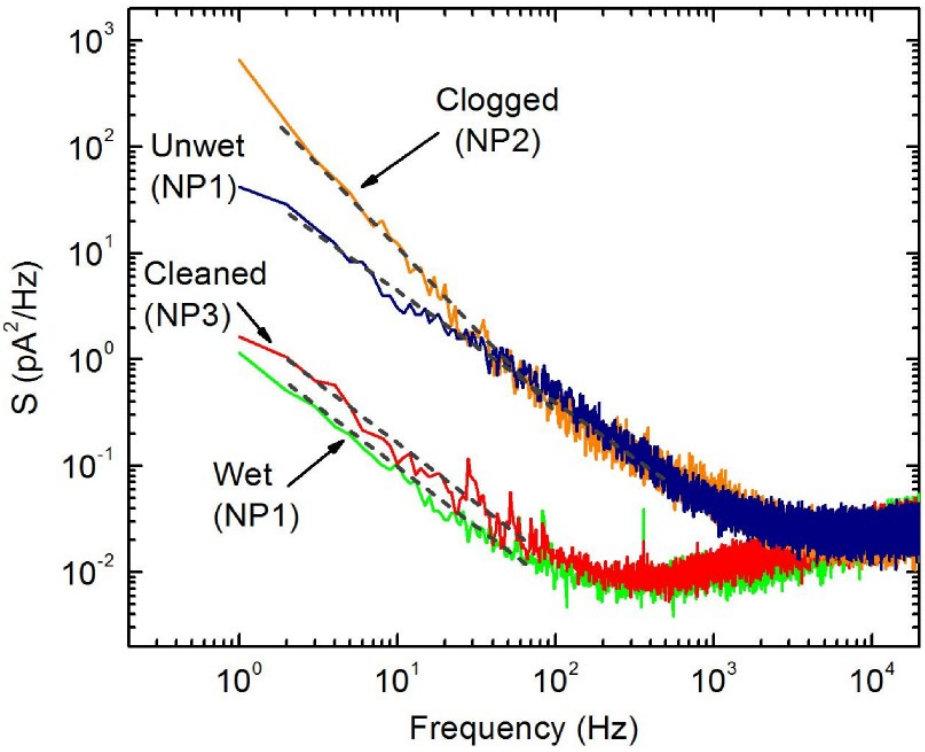

Figure 4.7 PSD versus frequency at 200 mV low-pass filtered at 100 kHz for three pores before and after treatment with high electric field pulses. Blue and green curves correspond to the same 7 nm pore (NP1) before and after complete wetting using 8 V pulses of 200 ms, respectively. The orange curve shows a typical PSD of a clogged, high-noise nanopore (NP2) that would typically be deemed unusable for experiment. The red curve shows the PSD of a previously clogged pore (NP3) that was cleaned using two 10 V pulses of 200 ms and regained low-noise characteristics. Dashed gray lines illustrate the $1/f^{\alpha}$ dependence of noise at low frequencies, where $0.94 < \alpha < 1.5$.

To illustrate the effectiveness of this method for reducing 1/f noise in incompletely wetted nanopores, an unused ~7 nm pore (as determined after TEM drilling) that failed to completely wet despite cleaning with piranha solution (blue curve in figure 4.6) was treated using 8 V pulses of 200 ms duration. While a total of 7 pulses were applied, nanopore conductance did not significantly change after the first one, indicating that a single pulse was sufficient to completely wet the pore. The PSD of the nanopore upon treatment (green curve) exhibits nearly two orders of magnitude reduction in low frequency noise, which varies as $1/f^{\alpha}$ with $\alpha = 0.94$, consistent with previously characterized low noise SiN

nanopores.[22] Moreover, the nanopore exhibited a conductance of 19.6 nS, appropriate for a 15 nm long cylindrical nanopore of 7 nm in diameter.

Interestingly, we find that once a nanopore has completely wetted, low noise characteristics are maintained throughout subsequent enlarging. Figure 4.8 shows current traces of a 10 nm pore (as determined after TEM drilling) before and after complete wetting and enlargement to 21 nm (G = 126 nS) using 8 V pulses of 2 s duration as described in section 4.1. Clearly, analysis of biomolecular translocation before treatment with high electric fields would be extremely challenging if not impossible, while the enlarged, treated pore exhibits substantial improvement in stability.

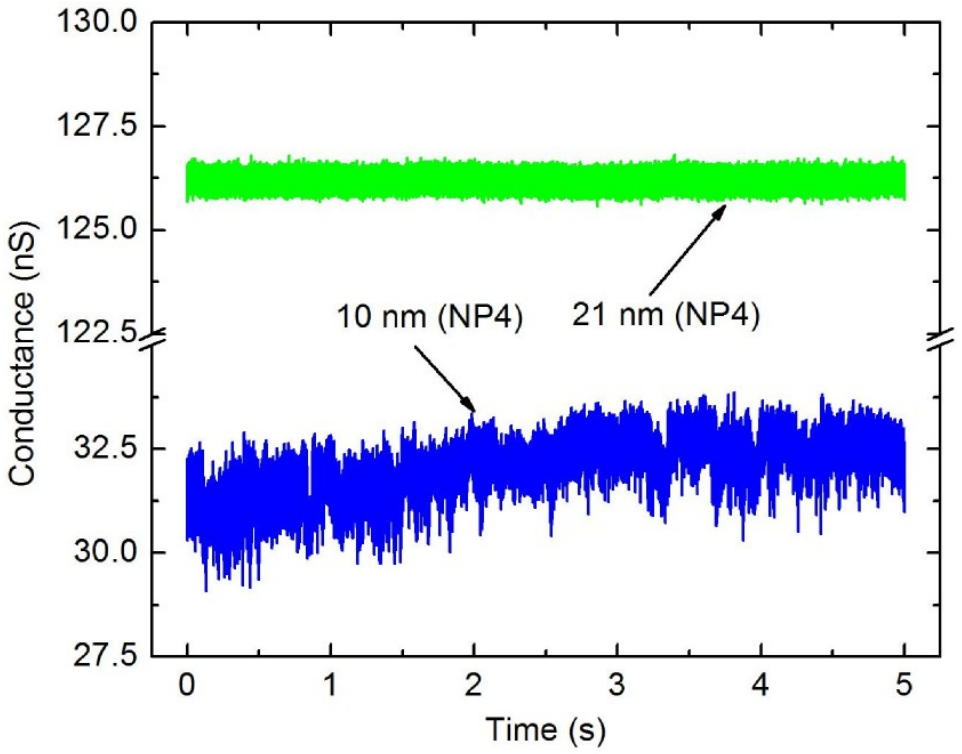

Figure 4.8 Current traces at 200 mV for an incompletely wetted 10 nm pore (blue, NP4) that was enlarged to 21 nm (green) using 8 V pulses of 2 s duration. Data was acquired at 250 kHz, low-pass filtered at 100 kHz and averaged every 5 data points for ease of viewing.

The complete wetting of a nanopore using a strong electric field has been previously observed and is understood as a lowering of the potential energy barrier for complete wetting of the pore via the alignment of the dipole moment of water vapour molecules [60,61]. However, the nanopores investigated in those studies were hydrophobically modified for the application of nanopore gating and were either fabricated with conical geometry in polymer films or were too large to be suitable for biomolecule detection. Moreover, the electric field strengths reached in these studies were over an order of magnitude less than those discussed here and a thorough investigation of the noise characteristics of treated nanopores was not performed. While high electric fields have also been previously used to facilitate wetting of SiN nanopores capable of detecting and characterizing DNA molecules,[28] to the best of the author's knowledge this study is the first to present data characterizing the process and experimental evidence revealing that low-frequency noise can be effectively reduced.

As discussed in section 3.4, it is often useful to represent the noise amplitude in terms of the I_{rms} noise. Figure 4.9 shows the noise amplitude at 200 mV of a nanopore before and after complete wetting using high electric field pulses at 200 mV as described section 4.1. Nanopores exhibiting I_{rms} above 15 pA RMS at a bandwidth of 5 kHz are considered "high-noise" making it very difficult to resolve translocating molecules from current signals. Of the 20 nanopores subjected to high field pulses in this study, 19 were completely wetted (i.e. exhibited a conductance consistent with that predicted from their geometry based on TEM imaging) and had a I_{rms} noise less than 15 pA at 5 kHz. As it is common to reject a large portion of nanopores due to high noise, current rectification and incomplete wetting, high electric field pulses show great promise as a means for reproducibly preparing functional low-noise nanopores for molecular recognition experiments.

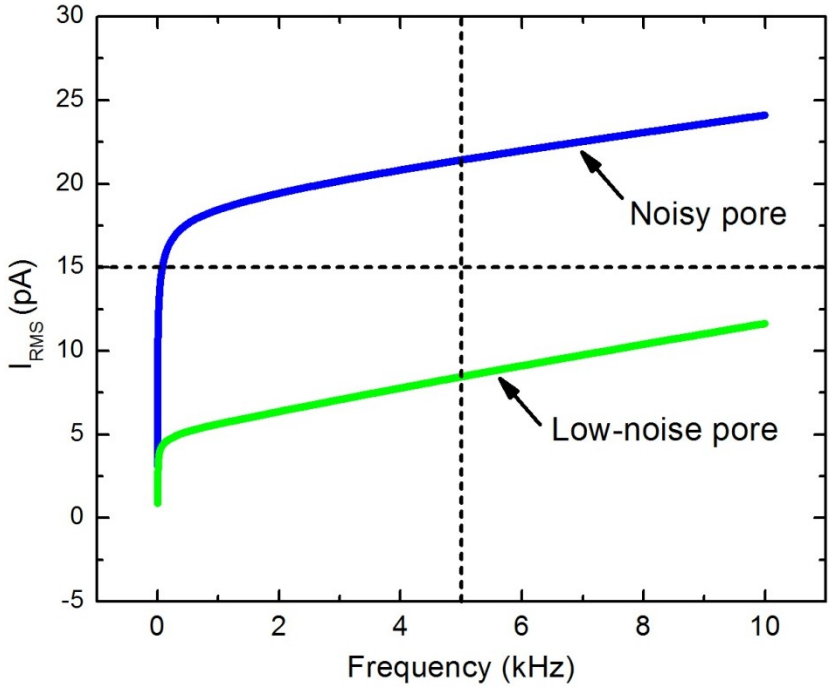

Figure 4.9. Current RMS noise amplitude as a function of the 1-10000 Hz bandwidth measured at 200 mV for the unwetted high-noise (blue) and wetted (green) 7 nm pore from figure 4.8. The horizontal dashed line at 15 pA RMS denotes the limit below which a nanopore is considered "low-noise" at 5 kHz.

5 PERFORMANCE VALIDATION USING DNA TRANSLOCATION

5.1 Analysis of DNA translocation

In order to validate the method of applying high electric fields for enlarging and lowering noise in solid-state nanopores, the ability of conditioned pores to detect the passage of single molecules was evaluated. Pores enlarged to diameters ranging from 10-35 nm (40-490 nS) were used to detect λ DNA (48.5 kbp dsDNA, purchased from New England BioLabs). Each pore was enlarged using 2 s pulses of 8-10 V as described in section 4.1. Upon enlarging each pore, both electrolyte reservoirs were flushed with 2 M KCl buffered at pH 8.0 prior to the addition of dsDNA. In order to more easily resolve transient current blockages due to translocating dsDNA molecules from baseline noise, 2 M electrolyte solution was used rather than 1 M KCl to increase signal-to-noise. For DNA experiments, current sampling was performed at 250 kHz and low-pass filtered at 100 kHz.

Prior to the addition of DNA to the system, control runs at 150 mV were performed. If the ionic current did not exhibit any transient current blockages for 2 min, λ DNA was introduced into one of the electrolyte reservoirs (referred to as the *cis* reservoir) at a working concentration of 1 μg/mL. Careful refluxing with a pipette ensured proper mixing of the DNA in the electrolyte reservoir. Figure 5.1 shows that at a bias of 150 mV, conductance spikes become clearly visible upon the addition of DNA as molecules are electrophoretically driven through 11 nm and 32 nm pores (87 nS and 432 nS, respectively). As expected for nanopores of these diameters, the inset of figure 5.1 shows multiple quantized blockage depths corresponding to the translocation of folded and unfolded DNA molecules (as in figure 1.2).[16] While translocation of molecules was observed at a rate of ~0.4 Hz, 600-700 events were recorded over the course of an experiment. Transient current blockages were

considered translocation events if they exceeded a user-defined threshold deviation from the open-pore baseline current.

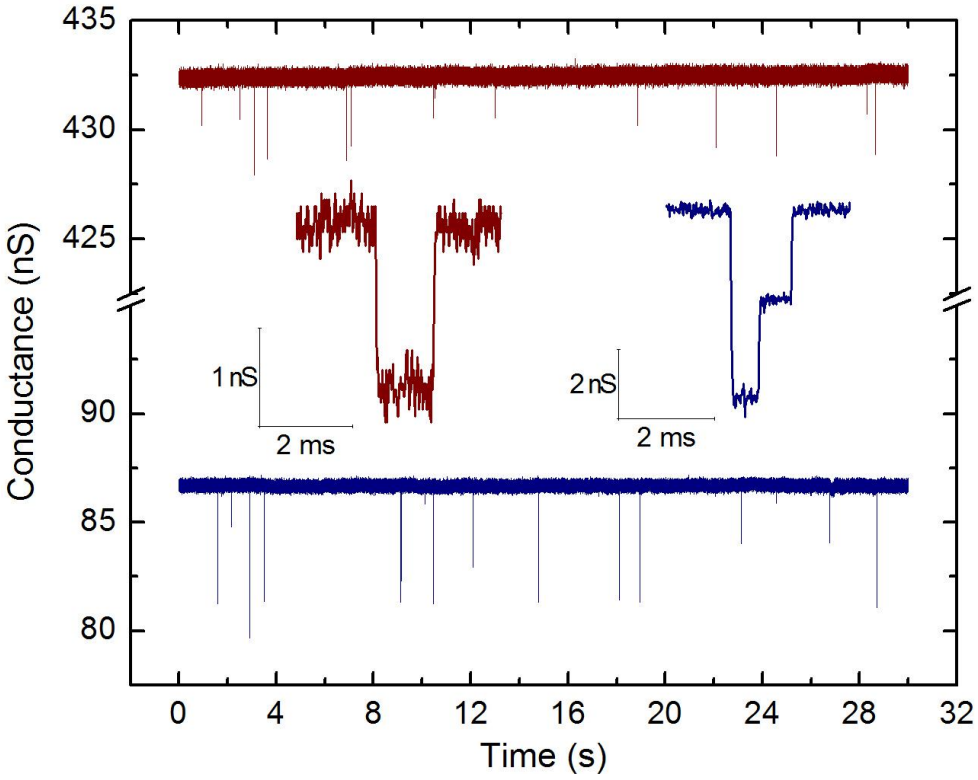

Figure 5.1 Detection of dsDNA using pores enlarged to 11 nm (87 nS, blue) and 32 nm (432 nS, red). Upon introduction of λ DNA and applying a 150 mV bias, current blockades appear in discreet quantized amplitudes corresponding to the translocation of zero, one and two dsDNA strands through the pore (inset). Current data was filtered using a 10 kHz low-pass Bessel filter for display.

Figure 5.2 shows a histogram of the nanopore conductance during translocation events, the equidistant separation of peaks in histograms of the nanopore conductance during translocation events confirms the presence of multiple discrete blockage states during translocation. We note that the reduction of 1/*f* noise in the open pore current signal, a result of the enlarging process, produces histograms with easily resolvable peaks. Furthermore, while nanopores would eventually clog throughout the course of a translocation experiment, low-noise open pore conductance values were often regained with short (100-200 ms) pulses

of 6-10 V. Nanopore rejuvenation for further experimentation through treatment with high electric fields is thus of great benefit for improving the efficiency and lifespan of nanopores.

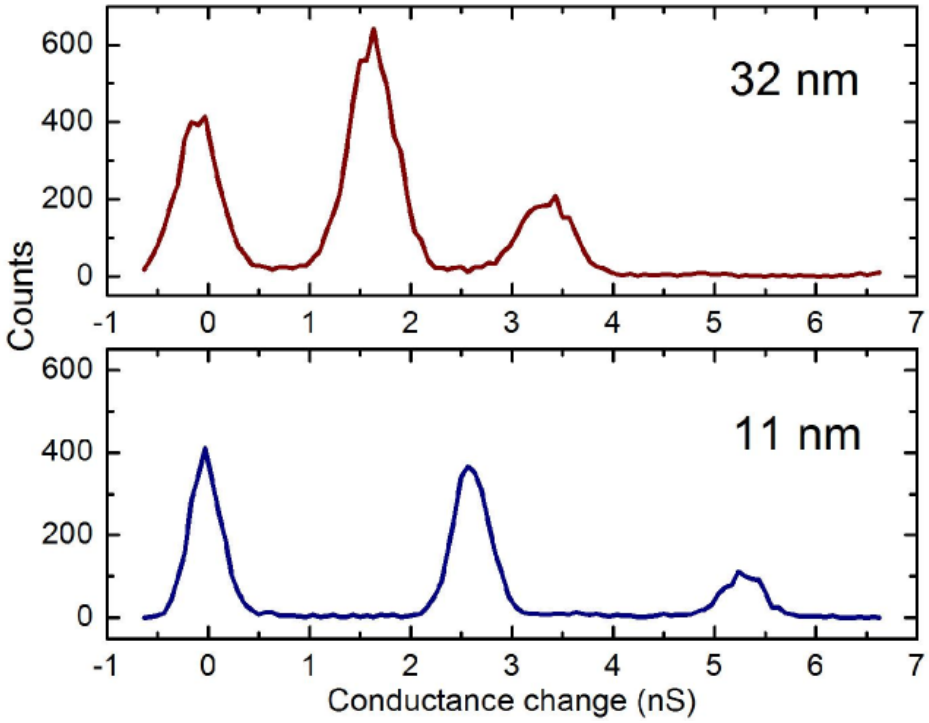

Figure 5.2 Histograms of the event conductance levels for DNA translocation events through the nanopores shown in figure 5.1. Peaks corresponding to the quantization of conductance blockades during translocation are clearly resolved at multiples of 1.7 nS and 2.6 nS for the 32 nm and 11 nm pores, respectively.

5.2 Geometrical analysis of treated nanopores using translocation depth

Interestingly, the change in conductance of ΔG = 1.7 nS produced by dsDNA translocating through the 32 nm pore is smaller than that of ΔG = 2.6 nS for the 11 nm pore. This is consistent with the model described by Kowalczyk, *et al.* [52] describing the increased role of access resistance in determining the change in nanopore conductance upon the translocation of dsDNA through large pores. The change in conductance can be modeled as shown in equation 5-1,

$$\Delta G = G(d) - G(d_{\text{with DNA}}) \qquad 5\text{-}1$$

where, G is given by equation 3-1 and $d_{\text{with DNA}}$, given by 5-2, is the effective diameter of the pore containing dsDNA of diameter d_{DNA} = 2.2 nm.

$$d_{\text{with DNA}} = \sqrt{(d^2 - d_{\text{DNA}}^2)} \qquad 5\text{-}2$$

Careful examination of equation 5-1 reveals that rather than observing a constant ΔG for translocating DNA through pores of varying open-pore conductance values, ΔG decreases as the diameter of the nanopore is increased. This is a result of the increased role of access resistance in determining the overall resistance of the nanopore system. This provides strong evidence supporting the claim that nanopores are in fact being enlarged by exposure to high electric field pulses. If the pore was not being enlarged or if multiple nanopores were present, ΔG would remain constant for different open-pore conductance values. As a definite trend of decreasing ΔG is noticed for higher conductance pores, access resistance is playing a more dominant role, a direct result of nanopore growth.

With measurements of both open-pore conductance and ΔG values translocation molecules of a known size, it is possible to calculate experimental values of l_{eff} assuming cylindrical geometry. Fits to equations 5-1 and 5-2 yield effective pore length of 11-16 nm for enlarged nanopores. This result agrees well with the assumed pore length of 15 nm from section 3.3, showing that enlarged nanopores have similar geometry to those produced by TEM.[52]

6 PRELIMINARY RESULTS: DNA-PROTEIN COMPLEX DETECTION

As mentioned in chapter 1, the majority of nanopore investigations to date have focused on the analysis of nucleic acids and improving electrical measurements for the purpose of DNA sequencing.[11] A small portion of the literature examines the translocation of proteins through solid-state nanopores, and a smaller portion still the simultaneous detection of proteins and DNA. The latter, however, have shown that it is possible to identify not only the presence of many randomly bound proteins such as RecA,[62] but single molecules bound at sequence-specific locations along a DNA strand by taking advantage of the recognition sites of peptide nucleic acids (PNAs)[63] and restriction enzymes.[64] While such methods are limited to the study of proteins with known DNA binding sequences and are thus not particularly useful for diagnostic applications, they highlight the ability of solid-state nanopores to detect the presence of individual proteins bound to a DNA scaffold. As such, solid-state nanopores can be implemented as a tool for sensing the presence of specific biomarkers. This chapter discusses a method by which this ability can be exploited for the development of a nanopore-based diagnostic tool for the detection of disease biomarkers from a tissue sample. Such a device could in theory screen panels of biomarkers for diagnosis, monitoring of disease progression and prognosis. It could also provide rapid analysis at relatively low cost, as well as eliminate cumbersome amplification and conversion steps required by current methods such as PCR and Sanger sequencing.

6.1 Biomarker detection scheme

As the noise and bandwidth limitations of solid-state nanopores currently prevent the direct identification of translocating proteins in an unknown sample, a novel method of identifying proteins based on current signatures from solid-state nanopores was developed.

In this scheme, specific biomarker proteins can be isolated from a sample by taking advantage of the specificity of protein-antibody interactions and subsequently detected using a nanopore. For example, standard biochemical techniques could be used to functionalize a strand of single- or double-stranded DNA which could then be conjugated to a protein or antibody (Ab) specific to the biomarker of interest.[65] Upon introduction of the sample, this DNA scaffold would selectively bind to the target molecule, essentially tagging it for identification.

In a nanopore experiment, the target biomarker of interest could be identified by the characteristic current blockade corresponding to the translocation of the DNA-target complex. In this scheme, the use of a DNA scaffold would both increase the charge density of the biomarker complex to aid translocation and provide a means of further differentiating targets of interest from a mixture. In theory, the bulky complex could be distinguished from translocation of the DNA scaffold alone to determine the presence or absence of a target, which would in turn be easily distinguished from unbound protein in a sample. A hypothetical schematic of such a detection scheme is described in figure 6.1, where the translocation signal of a bare DNA-receptor scaffold in the absence of target in a sample (figure 6.1a) could be distinguished that from the DNA-target complex (figure 6.1b).

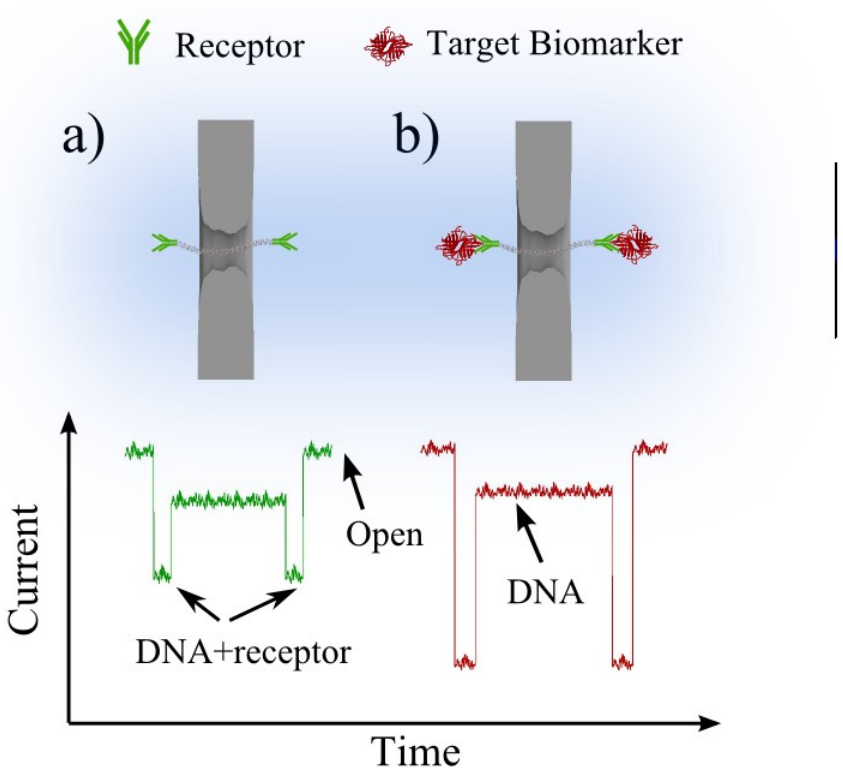

Figure 6.1 Schematic of hypothetical complex detection using solid-state nanopores. Using DNA-receptor scaffolds, current blockades upon the translocation of complexes could be used to determine the absence (a) or presence (b) or target molecules in a sample.

6.2 Proof-of-concept protein detection

In order to determine the feasibility of biomarker detection for disease diagnosis, it was first necessary to perform a proof-of-concept experiment. The goals of this trial were twofold: to design and optimize a procedure for functionalizing a DNA scaffold and protein complex, and to determine the ability of the conditioned nanopores to resolve proteins bound to the scaffold. An avidin-derivative, neutravidin, was chosen as a test target molecule as it is commercially available at reasonable cost and is a common analyte used in nanopore-based protein assays, providing a good benchmark with which results could be compared. This tetrameric protein, measuring ~5.6 x 5 x 4 nm, consists of four sub-units and binds very tightly to biotin in one of the strongest known protein-ligand interactions ($K_D \sim 10^{-15}$ M).[66]

Furthermore, neutravidin has near neutral charge under the experimental conditions used in our experiments (pI = 6.3), whereas its parent and sister proteins avidin and streptavidin are respectively highly cationic (pI = 10.5) and anionic (pI ~ 5). Strongly negative charge was undesirable as it was thought that electrostatic repulsion with negatively charged DNA would impede conjugation, whereas positively charged avidin would be cause conglomeration of multiple DNA strands and clogging at the negatively charged nanopore walls. Indeed, gel electrophoresis experiments attempting to characterize DNA-avidin binding showed evidence of massive aggregates unable even to enter agarose gel pores (data not shown). The considerable strength of the neutravidin-biotin interaction was also an attractive feature of the protein: as biotinylated ssDNA is commercially available, this interaction could be exploited in the formation of the DNA-neutravidin complex.

6.2.1 Double-stranded DNA scaffold generation using polymerase chain reaction

While various attachment locations were investigated, functionalizing DNA with biotin receptors proved most efficient at the ends of DNA strands. This was done amplifying segments of ds λ-DNA by polymerase chain reaction (PCR) using biotinylated primers to produce 5kbp dsDNA with a biotin at each 5' terminus.[67] This is a common technique by which segments of a strand of DNA (template) are amplified through the activity of a polymerase that incorporates deoxynucleotide triphosphate (dNTP) molecules into a ssDNA segment complementary to the template. The region of amplification (amplicon) is defined by the primer sequences (ssDNA ~10-30 bases in length) used to initiate polymerase activity. The 5'-biotinylated primers used here were 20 bases in length and spaced 5kbp apart on the λ-DNA sequence. A 5 kbp amplicon was chosen as it was long enough to be detected by the nanopore but small enough to be efficiently amplified by

PCR. Great care was taken to choose primer sequences that minimized self-interaction and hairpin formation using the Integrated DNA Technologies (IDT) OligoAnalyzer tool in order to maximize PCR efficiency and determine the annealing temperature. While PCR is typically performed on small (<1 kbp) amplicons, a polymerase enzyme specially engineered for amplifying segments of up to 20 kbp was used (Phusion High Fidelity Polymerase, Finnzymes F-530). A description of the primer sequences can be found in Appendix II.

PCR reaction conditions were optimized by first following the polymerase manufacturer's recommendations for a 50 μL reaction and tweaking the annealing temperature, extension times and DNA/primer/polymerase concentrations. Gel electrophoresis using 1% agarose gel run at 100 V and stained with EtBr was used to characterize each reaction. Figure 6.2 shows one such agarose gel, where a control run was compared with various reaction conditions. Clearly, with exception of lane 5 which uses already-amplified PCR product as a template, all of the reactions shown produce well-defined bands at the expected 5kbp. While bands 1-4 appear blurred, this is an effect of improper gel casting and sample introduction. Increasing extension time to 1 min/bp (not shown) did not noticeably improve yields, so in order to conserve reaction materials and save reaction time, the optimized reaction conditions were found to be those recommended by the manufacturer (lane 1), which are given in Appendix II.

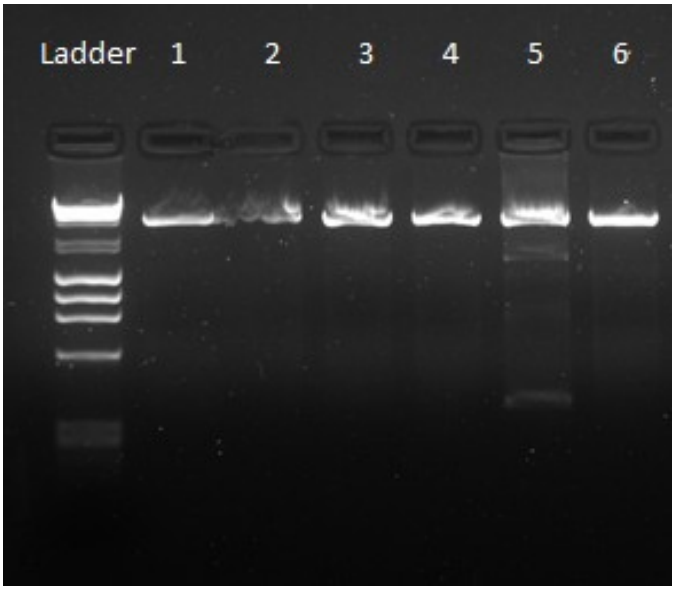

Figure 6.2 Image of the agarose gel used to characterize PCR optimization of 5kb amplicon. The 1% agarose gel stained with EtBr was made with 1X TAE buffer and ran with 1X TAE for ~30 min at 100 V. The first lane shows a 1 kb DNA length standard ladder. Lanes 1 and 2 are PCR products following Finnzyme's recommended amplification protocol using the manufacturer's λ-DNA (control) and aliquoted λ–DNA purchased from New England Biolabs as templates, respectively. Default annealing temperature was 64℃ and extension time was 2.5 min (30 s/kb). Lanes 3 and 4 were performed as lane 2 but with an annealing temperature of 60℃ and 68℃, respectively. Lanes 5 and 6 were run as lane 2 but using, respectively, 2 μL of the PCR product of lane 1 and double the concentrations of starting DNA, primers, dNTPs and polymerase. All reactions were performed using the biotinylated primers described in Appendix II.

6.2.2 Template purification and concentration

In order to form the desired DNA-avidin complex, purification of the PCR product from the reagents and primers used was crucial. Not only can the detergents used adhere to the nanopore walls and severely degrade electrical signals, but leftover biotin primers can interfere with concentration measurements and the coupling of functionalized DNA and target by occupying the neutravidin binding sites. As nanopore experiments typically require DNA concentrations of ~1 ng/uL, it was also necessary to obtain pure DNA scaffold in concentrations of > 20 ng/uL in order to ensure sufficient concentrations when diluted in electrolyte solution. In order to obtain the purest possible scaffold, several purification methods were compared, with success determined using a Nanodrop1000 spectrophotometer

by the concentration of DNA yielded and purity of the sample, as determined by ratio of the absorbance of the sample at 260 nm to 280 nm (260/280). For pure proteins, 260/280 ~ 1.8, while readings of << 1.8 typically indicate the presence of protein or alcohol contamination. The results of the various purification protocols are summarized in Table 1.

Firstly a gel extraction kit (Qiagen cat no. 28704) was attempted, in which the PCR product is run through an agarose gel as in figure 6.2 and the 5 kbp band excised. The benefit of this technique is that only DNA of desired length is obtained, as any bands not excised for further purification are removed from the sample. The band of gel is then dissolved and added to silica beads which bind DNA and is spun down to form a pellet. The supernatant is removed and the beads washed with alcohol to remove any residual contaminants. The DNA is then eluted by using TE buffered at pH 8.5, as per the manufacturer's protocol. However, as seen from table 1, not only does the gel extraction method provide a very poor yield of DNA, PCR products purified using the gel extraction method show significant contamination of either proteins or residual alcohols from the extraction process.

The second purification method attempted was isopropanol (IPA) precipitation. As in the protocol described by Cseke, *et al*.,[68] this method relies on the relative insolubility of nucleic acids in IPA for the precipitation of DNA from the PCR reaction mixture. While some primers will also precipitate, their small sizes make them considerably more soluble and can therefore be removed when the mixture is spun in a centrifuge. The resultant pellet following an EtOH wash can be resuspended in aqueous buffer. While some precipitations were quite successful, yielding over 90 ng/μL concentrations, the method was found to be difficult to perform consistently, with about 50% yielding little to no DNA following

resuspension, as indicated by the relatively low concentration value in Table 1. This was likely due to accidental removal of the DNA pellet during wash steps. Due to the unpredictable yields of valuable PCR products and slight evidence of contamination, this method was also deemed unfit for purifying the DNA scaffold.

The final purification method attempted was a commercial PCR cleanup spin column (GeneJet cat. no. K0701). While the least labour-intensive method investigated, it also proved the most efficient. This kit consisted of a thin silica membrane in a 2 mL mini-centrifuge tube that selectively adsorbs dsDNA molecules ranging from 0.1-10 kbp while allowing polymerase molecules, reagents and small DNA fragments such as primers to pass through. Following an ethanol wash step, trapped DNA is eluted in a high pH buffer (pH = 8.5). As indicated in Table 1, DNA scaffold yields were ideal for subsequent dilution in electrolyte buffer for nanopore experiments, and the 260/280 ratio shows little to no protein contamination. PCR cleanup spin columns were therefore used as the method of choice for purification of DNA scaffolds for further processing and nanopore measurements.

Table 1 Comparison of PCR product purification methods

Purification Method	Average DNA concentration (ng/uL)	260/280
Gel extraction	5.5	1.5
IPA precipitation	34.4	1.7
Spin column	50.0	1.8

6.2.3 Preparation of DNA-neutravidin scaffolds

As residual primers may be left over after purification of the PCR products, the optimal ratio of neutravidin to purified DNA must be determined to ensure complete saturation with neutravidin of the DNA scaffold. This was done by creating stock solutions of 10 ng/μL and 1 mg/μL stock solutions of neutravidin by diluting in TE buffered at pH 8.5 and mixing the appropriate volumes of protein to 300 ng of purified DNA. As DNA scaffold are doubly biotinylated, a 1:1 mixture involves adding twice the amount of moles of neutravidin than DNA. In order to cover a broad range of ratios, 1:1, 2:1, 10:1, 100:1 and 1000:1 mixtures neutravidin:biotin were created. As neutravidin is tetravalent (capable of binding 4 biotin molecules) and each DNA molecule is capable of binding two avidin molecules, in all cases, care was taken to ensure that DNA was added to neutravidin solution slowly in order to encourage saturation of the biotinylated DNA. The samples were then incubated at room temperature for 1 hr. Subsequent gel electrophoresis at 100 V for 30 min of the various mixtures is shown in figure 6.3. Control purified DNA and mixtures of <100:1 the gel shows evidence of non-specific PCR product at ~600 bp that was not removed from the PCR mixture during purification. For high neutravidin:biotin ratios, however, this non-specific product is not present. Furthermore, the 5 kbp bands in these lanes exhibit slightly less migration and minor blurring above the bands. It is believed that this is due to the increased mass and lower charge density of the DNA-neutravidin complex, as expected for successful conjugation. The blurring may also be due to conjugation of the smaller non-specific bands, which may not carry sufficient charge density to overcome the bulk and mass of tethered neutravidin, causing it to appear above the 5 kbp band. As >100:1 excesses of neutravidin show evidence of conjugation, subsequent assays use this ratio of neutravidin:biotin.

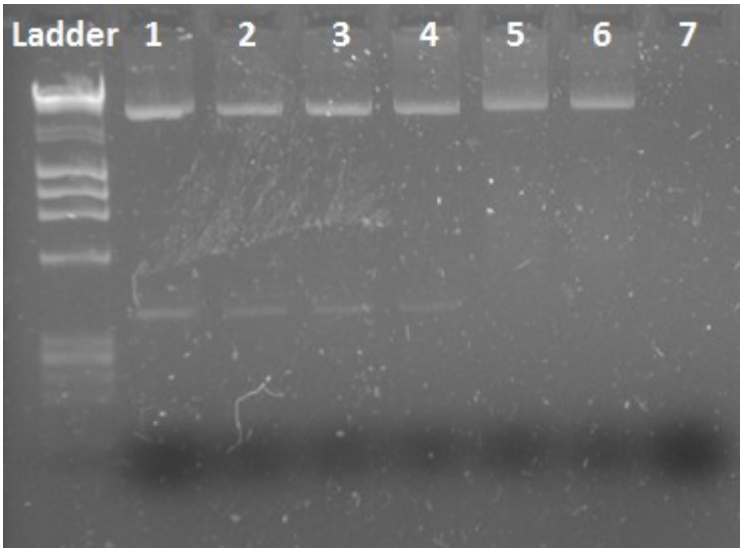

Figure 6.3 Optimizing neutravidin:biotin mixing ratios. A 1% agarose gel stained with EtBr run at 100 V for 30 min was used to determine the optimal ratio of neutravidin to DNA for efficient multiplex production. Each lane contains 300 ng of 5kbp purified DNA scaffold in 10 μL TE buffered at pH 8.4. Lanes 1 and 7 contain control DNA scaffold and 8 μg of neutravidin, respectively. Lanes 2-6 contain neutravidin:biotin ratios of 1:1, 2:1, 10:1, 100:1 and 1000:1.

6.2.4 Nanopore analysis of purified DNA scaffolds and complexes

Before attempting to detect the DNA-neutravidin complex, the nanopore system's ability to detect the bare 5 kbp scaffold was investigated. As in chapter 5, nanopores are conditioned for low noise using 200 ms pulses of 8 V to completely wet the nanopore and lower 1/f noise prior to the introduction of DNA. As expected, the low noise nanopores readily exhibited well-resolved spikes corresponding to the translocation of DNA molecules, illustrating both the effectiveness of the PCR for creating 5 kbp biotinylated scaffolds and the efficiency of the PCR cleanup columns for purifying the DNA.

As an attempt to slow DNA translocation for the potential detection of proteins bound to the DNA, the effect of varying the electrolyte salt on translocation speed was investigated. It has recently been observed experimentally that the use of lithium chloride (LiCl) can slow DNA translocation through a solid-state nanopore.[18] This is thought to be

due to an increased shielding of the negative charge of DNA through an increased lifetime of the Li-DNA bond, lessening the electrophoretic force exerted on the DNA molecule. Figure 6.4 shows histograms of the dwell times of the dsDNA scaffolds in both 1 M KCl and 1 M LiCl electrolyte solutions through pores of 9.4 nm and 4.3 nm, respectively. While the most probable dwell time of 5 kbp DNA in KCl is 60 μs (corresponding to a velocity of ~28 nm/μs), it is 90 μs for 1 M LiCl (18 nm/μs). It should be noted that while LiCl appears to slow translocation, this increase in translocation time may also be partially affected by the larger nanopore diameter.

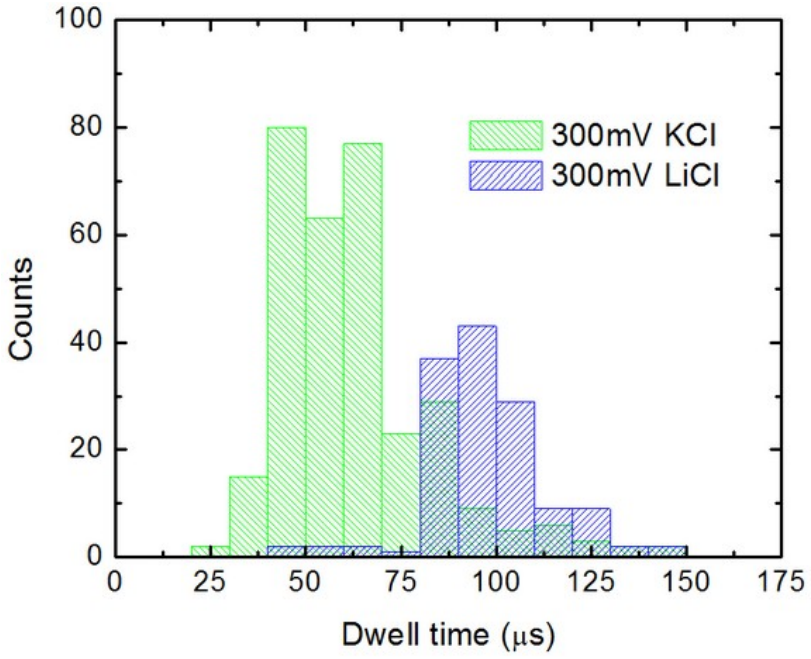

Figure 6.4 Histogram of translocation dwell times of purified 5 kbp biotinylated DNA scaffold in two ionic solutions through two different electric field-conditioned nanopores. The most probable translocation time through a 9.4 nm pore in 1 M KCl is 60 μs, while for a 4.3 nm pore in 1 M LiCl is 90 μs.

Neutravidin-DNA complexes were then formed as in section 6.3 using a 100:1 ratio of neutravidin:biotin and introduced into the *cis* chamber of the nanopore cell at a DNA concentration of 1 ng/μL. Despite the success of enlarging nanopores and achieving low-

noise characteristics for the detection of 5 kbp DNA scaffolds, acquisition of translocation data for the multiplex was not possible for the 5 nanopores attempted. As shown in figure 6.5 for nanopores of 79 nm and 67 nm, nanopores would become clogged almost immediately following the application of a transmembrane potential. While applying short pulses of 6-8 V as in section 4.2 was usually sufficient to temporarily clear the obstruction, the pore would immediately clog again, sometimes irreversibly.

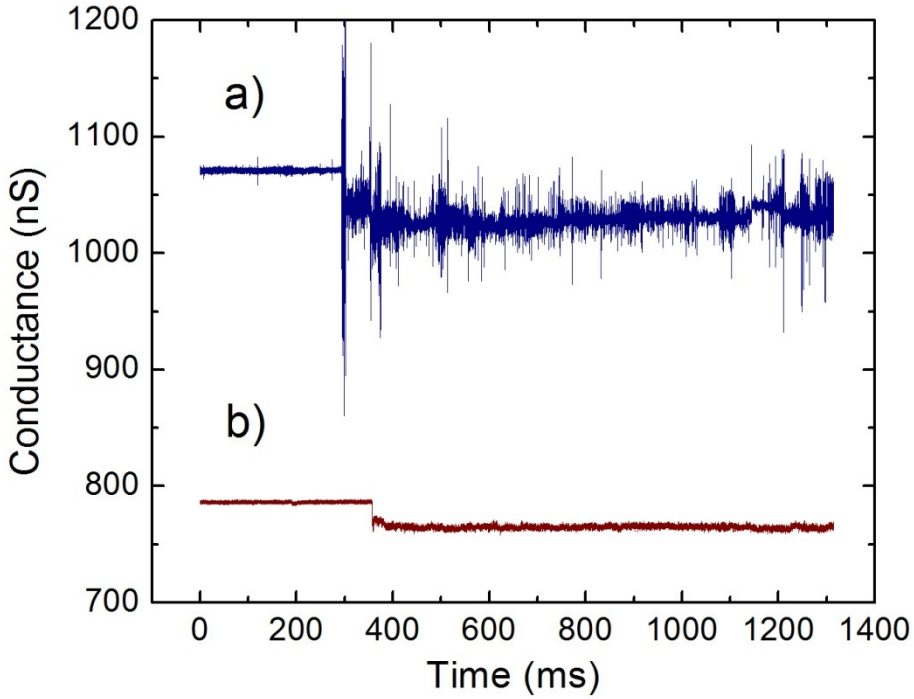

Figure 6.5 DNA-neutravidin complexes clogging a nanopore at 200 mV. While a relatively low-noise current signal is achieved through nanopore conditioning with electric fields, nanopores become almost instantly clogged upon the application of an electric potential, despite the nanopores having enlarged diameters of 79 nm (a) and 67 nm (b).

It is possible that the clogging issues observed during multiplex measurements are due to adsorption of free proteins to the nanopore walls.[24] However, adjusting the electrolyte pH from 5 to 8 in order to vary the charge of neutravidin molecules in solution did not provide any more success. It is more likely that instead of making single DNA complexes bound to two neutravidin molecules, large networks of concatamers were

generated that were too large to pass through even very large nanopores. Despite the care taken in sample preparation, there is still a large likelihood that this could not be avoided due to the tetrameric nature of neutravidin and the doubly biotinylated DNA strands.

6.3 Outlook

As neutravidin proved a poor test protein for a proof-of-concept experiment, future experiments geared towards the detection of DNA-protein complexes for medical diagnostics will address the challenges encountered in this study. Primarily, this will involve the development of a new method of creating complexes for biomarker detection that eliminates the possibility of concatamerization that was observed with tetrameric avidin proteins.

One potential avenue for achieving this is to utilize the monovalent nature of monoclonal antibodies for the detection of biomarkers. While a variety of techniques exist to covalently bond proteins and antibodies to functionalized DNA,[69] it is imperative that the method used offer well-defined stoichiometric compositions and not interfere with the active binding site of the antibody. A promising cross-linking strategy for achieving complex formation while avoiding these issues is maleimide chemistry, which can covalently link antibody thiol groups with amine-functionalized DNA.[65] The advantage of this technique is that specific regions of the antibody can be targeted for cross-linking, leaving an active binding region for protein recognition, and can allow coupling of long dsDNA fragments. This would allow for a similar scaffold generation using PCR as described here, substituting biotin for amine-modified PCR primers.

An exciting alternative to standard antibodies for binding biomarkers of interest is the use of antibody fragments (F_{ab}).[70] These molecules are comprised of the active binding region of antibodies and can be synthesized in the laboratory. What is particularly attractive of this approach is that they are smaller than standard antibodies (~50 kDa compared to ~150 kDa) and can be specifically engineered to provide maleimide-active binding sites that do not interfere with ligand binding. This both reduces their size in order to improve resolution of F_{ab} and F_{ab}-target in nanopore current signals as well as ensures a 1:1 binding ratio with functionalized DNA scaffolds.

While the use of F_{ab} show great promise for biomarker detection, an attractive alternative to forming multiplexes lies in the use of nucleic acid aptamers. Typically short (10-100 bases) strands of ssDNA, nucleic acid aptamers are engineered with a specific genetic sequence that causes them to fold into a distinct three-dimensional conformation.[71] As such, aptamers offer molecular recognition properties similar to antibodies allowing them to bind specifically to molecular targets such as proteins. Aptamers would be particularly advantageous for tethering biomarkers to a DNA scaffold as they allow for binding to distinct locations along the DNA backbone through specific base pair interactions, as well as provide a more robust alternative to antibodies as they are made of only nucleic acids. This would also eliminate the need for cross-linking antibodies or F_{ab} to the DNA scaffold, reducing sample preparation time and improving overall yields.

7 CONCLUSION

Nanopore technologies have emerged as a versatile tool for probing the properties and activity of single biomolecules for a host of applications. The superior durability, ability to control size and compatibility with microfabrication and wafer-scale technologies of solid-state nanopores make them an attractive alternative to their biological counterparts. Despite their advantages, however, the difficulty associated with size tuneability, high noise properties and low fabrication yields prevent the platform from realizing its potential in many applications such as genotype sequencing, or, in the case of this thesis, the identification of target biomolecules for the purpose of disease diagnostics.

In order to address these challenges and realize the goal of disease biomarker detection, this thesis proposes a method of conditioning TEM-drilled nanopores fabricated before use that can simultaneously offer control over nanopore size and improve current noise characteristics. By applying short, high electric field pulses, nanopore size can be increased in sub-nanometer increments which can be monitored in real-time in an automated fashion to achieve any desired diameter. Similarly, low-frequency 1/f noise can be reduced by up to three orders of magnitude for the increased precision and ability to detect translocation. Of particular advantage of this technique is that it is performed entirely *in situ* under experimental conditions, increasing the accuracy of size tuning and reducing the cost and time associated with fabrication. As over 90% of conditioned nanopores exhibit desirable electrical characteristics, this method is useful not only for the detection of large molecular complexes but is of great benefit for any solid-state nanopore application.

Given the success of the conditioning method, solid-state nanopores can be used for identifying the presence of target analytes in a sample. As a proof of concept, double-

stranded DNA scaffolds were produced by polymerase chain reaction that exploited the well-characterized strength of the neutravidin-biotin interaction for tethering a protein to the DNA backbone. While actual detection of the complex was not possible due to the properties of the target molecule, purification and subsequent characterization of the DNA scaffold using both gel electrophoresis and nanopore detection demonstrated the feasibility of the approach given a suitable biomarker target. As such, future investigations will explore the use of monoclonal antibodies, antibody fragments and nucleic acid aptamers for the detection of biomarkers in a sample.

In summary, the methods described in this thesis have enabled the reliable preparation of solid-state nanopores for single-molecule studies. This can result in a wide-ranging impact on the field through the reduction of cost associated with nanopore fabrication. As such, this work will almost certainly play a role in the development of solid-state nanopore methods as a single-molecule sensing platform to a valuable medical diagnostic tool for personalized medicine and the rapid, bedside detection of disease biomarkers.

REFERENCES

(1) Guttmacher, A. E.; Collins, F. S. *N. Engl. J. Med.* **2002**, *347*, 1512–1520.
(2) Shastry, B. S. *J. Hum. Genet.* **2007**, *52*, 871–880.
(3) Whibley, C.; Pharoah, P. D. P.; Hollstein, M. *Nature Reviews Cancer* **2009**, *9*, 95–107.
(4) Ingelman-Sundberg, M.; Oscarson, M.; McLellan, R. A. *Trends Pharmacol. Sci.* **1999**, *20*, 342–349.
(5) Ross, J. S.; Fletcher, J. A. *Stem Cells* **1998**, *16*, 413–428.
(6) Abbs, S.; Bobrow, M. *J Med Genet* **1992**, *29*, 191–196.
(7) Branton, D.; Deamer, D. W.; Marziali, A.; Bayley, H.; Benner, S. A.; Butler, T.; Ventra, M. D.; Garaj, S.; Hibbs, A.; Huang, X.; Jovanovich, S. B.; Krstic, P. S.; Lindsay, S.; Ling, X. S.; Mastrangelo, C. H.; Meller, A.; Oliver, J. S.; Pershin, Y. V.; Ramsey, J. M.; Riehn, R.; Soni, G. V.; Tabard-Cossa, V.; Wanunu, M.; Wiggin, M.; Schloss, J. A. *Nature Biotechnology* **2008**, *26*, 1146–1153.
(8) Deamer, D. W.; Akeson, M. *Trends Biotechnol.* **2000**, *18*, 147–151.
(9) Lemay, S. G. *ACS Nano* **2009**, *3*, 775–779.
(10) Bezrukov, S. M.; Vodyanoy, I.; Parsegian, V. A. *Nature* **1994**, *370*, 279–281.
(11) Venkatesan, B. M.; Bashir, R. *Nature Nanotechnology* **2011**, *6*, 615–624.
(12) Maglia, G.; Restrepo, M. R.; Mikhailova, E.; Bayley, H. *Proc. Natl. Acad. Sci. U.S.A.* **2008**, *105*, 19720–19725.
(13) Dekker, C. *Nature Nanotechnology* **2007**, *2*, 209–215.
(14) Craighead, H. *Nature* **2006**, *442*, 387–393.
(15) Rosenstein, J. K.; Wanunu, M.; Merchant, C. A.; Drndic, M.; Shepard, K. L. *Nature Methods* **2012**, *9*, 487–492.
(16) Li, J.; Gershow, M.; Stein, D.; Brandin, E.; Golovchenko, J. A. *Nature Materials* **2003**, *2*, 611–615.
(17) Cockroft, S. L.; Chu, J.; Amorin, M.; Ghadiri, M. R. *J. Am. Chem. Soc.* **2008**, *130*, 818–820.
(18) Kowalczyk, S. W.; Wells, D. B.; Aksimentiev, A.; Dekker, C. *Nano Letters* **2012**, *12*, 1038–1044.
(19) Lieberman, K. R.; Cherf, G. M.; Doody, M. J.; Olasagasti, F.; Kolodji, Y.; Akeson, M. *J. Am. Chem. Soc.* **2010**, *132*, 17961–17972.
(20) Clarke, J.; Wu, H.-C.; Jayasinghe, L.; Patel, A.; Reid, S.; Bayley, H. *Nature Nanotechnology* **2009**, *4*, 265–270.
(21) Tabard-Cossa, V.; Wiggin, M.; Trivedi, D.; Jetha, N. N.; Dwyer, J. R.; Marziali, A. *ACS Nano* **2009**, *3*, 3009–3014.
(22) Tabard-Cossa, V.; Trivedi, D.; Wiggin, M.; Jetha, N. N.; Marziali, A. *Nanotechnology* **2007**, *18*, 305505.
(23) Keyser, U. F.; van der Does, J.; Dekker, C.; Dekker, N. H. *Review of Scientific Instruments* **2006**, *77*, 105105–105105–9.
(24) Niedzwiecki, D. J.; Grazul, J.; Movileanu, L. *J. Am. Chem. Soc.* **2010**, *132*, 10816–10822.
(25) Firnkes, M.; Pedone, D.; Knezevic, J.; Döblinger, M.; Rant, U. *Nano Lett.* **2010**, *10*, 2162–2167.
(26) Wei, R.; Gatterdam, V.; Wieneke, R.; Tampé, R.; Rant, U. *Nature Nanotechnology* **2012**, *7*, 257–263.
(27) Rotem, D.; Jayasinghe, L.; Salichou, M.; Bayley, H. *J. Am. Chem. Soc.* **2012**, *134*, 2781–2787.
(28) Wanunu, M.; Bhattacharya, S.; Xie, Y.; Tor, Y.; Aksimentiev, A.; Drndic, M. .
(29) Dorvel, B.; Sigalov, G.; Zhao, Q.; Comer, J.; Dimitrov, V.; Mirsaidov, U.; Aksimentiev, A.; Timp, G. *Nucleic Acids Res* **2009**, *37*, 4170–4179.
(30) Baker, M. *Nature Biotechnology* **2005**, *23*, 297–304.
(31) Dudley, J. T.; Butte, A. J. *Pac Symp Biocomput* **2009**, 27–38.
(32) Johnson, C. J.; Zhukovsky, N.; Cass, A. E. G.; Nagy, J. M. *Proteomics* **2008**, *8*, 715–730.
(33) Etzioni, R.; Urban, N.; Ramsey, S.; McIntosh, M.; Schwartz, S.; Reid, B.; Radich, J.; Anderson, G.; Hartwell, L. *Nat. Rev. Cancer* **2003**, *3*, 243–252.
(34) Lilja, H.; Ulmert, D.; Vickers, A. J. *Nature Reviews Cancer* **2008**, *8*, 268–278.
(35) Ramaswamy, S.; Tamayo, P.; Rifkin, R.; Mukherjee, S.; Yeang, C. H.; Angelo, M.; Ladd, C.; Reich, M.; Latulippe, E.; Mesirov, J. P.; Poggio, T.; Gerald, W.; Loda, M.; Lander, E. S.; Golub, T. R. *Proc. Natl. Acad. Sci. U.S.A.* **2001**, *98*, 15149–15154.
(36) Storm, A.; Chen, J.; Zandbergen, H.; Dekker, C. *Physical Review E* **2005**, *71*.
(37) Wu, M.-Y.; Krapf, D.; Zandbergen, M.; Zandbergen, H.; Batson, P. E. *Applied Physics Letters* **2005**, *87*, 113106.

(38) Wu, M.-Y.; Smeets, R. M. M.; Zandbergen, M.; Ziese, U.; Krapf, D.; Batson, P. E.; Dekker, N. H.; Dekker, C.; Zandbergen, H. W. *Nano Letters* **2009**, *9*, 479–484.
(39) Schneider, G. F.; Kowalczyk, S. W.; Calado, V. E.; Pandraud, G.; Zandbergen, H. W.; Vandersypen, L. M. K.; Dekker, C. *Nano letters* **2010**.
(40) Egerton, R. F.; Li, P.; Malac, M. *Micron* **2004**, *35*, 399–409.
(41) Egerton, R. F.; Wang, F.; Crozier, P. A. *Microscopy and Microanalysis* **2006**, *12*, 65–71.
(42) Bradley, C. R. *Calculations of atomic sputtering and displacement cross-sections in solid elements by electrons with energies from threshold to 1. 5 MV*.
(43) Barnes, J. R.; Hoole, A. C. F.; Murrell, M. P.; Welland, M. E.; Broers, A. N.; Bourgoin, J. P.; Biebuyck, H.; Johnson, M. B.; Michel, B. *Applied Physics Letters* **1995**, *67*, 1538–1540.
(44) van den Hout, M.; Hall, A. R.; Wu, M. Y.; Zandbergen, H. W.; Dekker, C.; Dekker, N. H. *Nanotechnology* **2010**, *21*, 115304.
(45) Storm, A. J.; Chen, J. H.; Ling, X. S.; Zandbergen, H. W.; Dekker, C. *Nat Mater* **2003**, *2*, 537–540.
(46) Prabhu, A. S.; Freedman, K. J.; Robertson, J. W. F.; Nikolov, Z.; Kasianowicz, J. J.; Kim, M. J. *Nanotechnology* **2011**, *22*, 425302.
(47) Li, Q.; Zhao, Q.; Lu, B.; Zhang, H.; Liu, S.; Tang, Z.; Qu, L.; Zhu, R.; Zhang, J.; You, L.; Yang, F.; Yu, D. *Nanoscale* **2012**, *4*, 1572–1576.
(48) Smeets, R.; Dekker, N.; Dekker, C. *Nanotechnology* **2009**, *20*, 095501.
(49) Smeets, R. M. M.; Keyser, U. F.; Dekker, N. H.; Dekker, C. *PNAS* **2008**, *105*, 417–421.
(50) Levis, R. A.; Rae, J. L. *Meth. Enzymol.* **1998**, *293*, 218–266.
(51) Dimitrov, V.; Mirsaidov, U.; Wang, D.; Sorsch, T.; Mansfield, W.; Miner, J.; Klemens, F.; Cirelli, R.; Yemenicioglu, S.; Timp, G. *Nanotechnology* **2010**, *21*, 065502.
(52) Kowalczyk, S. W.; Grosberg, A. Y.; Rabin, Y.; Dekker, C. *Nanotechnology* **2011**, *22*, 315101.
(53) Johnson, J. B. *Phys. Rev.* **1928**, *32*, 97–109.
(54) Hooge, F. N. *Physics Letters A* **1969**, *29*, 139–140.
(55) Smeets, R. M. M.; Keyser, U. F.; Wu, M. Y.; Dekker, N. H.; Dekker, C. *Phys. Rev. Lett.* **2006**, *97*, 088101.
(56) Pedone, D.; Firnkes, M.; Rant, U. *Anal. Chem.* **2009**, *81*, 9689–9694.
(57) Yusko, E. C.; Johnson, J. M.; Majd, S.; Prangkio, P.; Rollings, R. C.; Li, J.; Yang, J.; Mayer, M. *Nature Nanotechnology* **2011**, *6*, 253–260.
(58) Liebes, Y.; Drozdov, M.; Avital, Y. Y.; Kauffmann, Y.; Rapaport, H.; Kaplan, W. D.; Ashkenasy, N. *Applied Physics Letters* **2010**, *97*, 223105.
(59) Kim, M. J.; Wanunu, M.; Bell, D. C.; Meller, A. *Advanced Materials* **2006**, *18*, 3149–3153.
(60) Powell, M. R.; Cleary, L.; Davenport, M.; Shea, K. J.; Siwy, Z. S. *Nature Nanotechnology* **2011**, *6*, 798–802.
(61) Smirnov, S. N.; Vlassiouk, I. V.; Lavrik, N. V. *ACS Nano* **2011**, *5*, 7453–7461.
(62) Smeets, R. M. M.; Kowalczyk, S. W.; Hall, A. R.; Dekker, N. H.; Dekker, C. *Nano Lett.* **2009**, *9*, 3089–3096.
(63) Singer, A.; Wanunu, M.; Morrison, W.; Kuhn, H.; Frank-Kamenetskii, M.; Meller, A. *Nano Lett.* **2010**, *10*, 738–742.
(64) Zhao, Q.; Sigalov, G.; Dimitrov, V.; Dorvel, B.; Mirsaidov, U.; Sligar, S.; Aksimentiev, A.; Timp, G. *Nano Letters* **2007**, *7*, 1680–1685.
(65) Lapiene, V.; Kukolka, F.; Kiko, K.; Arndt, A.; Niemeyer, C. M. *Bioconjugate Chem.* **2010**, *21*, 921–927.
(66) Rosano, C.; Arosio, P.; Bolognesi, M. *Biomol. Eng.* **1999**, *16*, 5–12.
(67) Mullis, K. B.; Faloona, F. A. In *Recombinant DNA Part F*; Academic Press, 1987; Vol. Volume 155, pp. 335–350.
(68) Cseke, L. J.; Kaufman, P. B.; Kirakosyan, A.; Westfall, M. V. *Handbook of Molecular and Cellular Methods in Biology and Medicine, Third Edition*; Taylor & Francis, 2010.
(69) Saccà, B.; Niemeyer, C. M. *Chemical Society Reviews* **2011**, *40*, 5910.
(70) Bradbury, A. R. M.; Sidhu, S.; Dübel, S.; McCafferty, J. *Nat. Biotechnol.* **2011**, *29*, 245–254.
(71) Bock, L.; Griffin, L.; Latham, J.; Vermaas, E.; Toole, J. *Nature* **1992**, *355*, 564–566.

APPENDIX I – DESIGN OF CELL HOUSING AND SHIELD

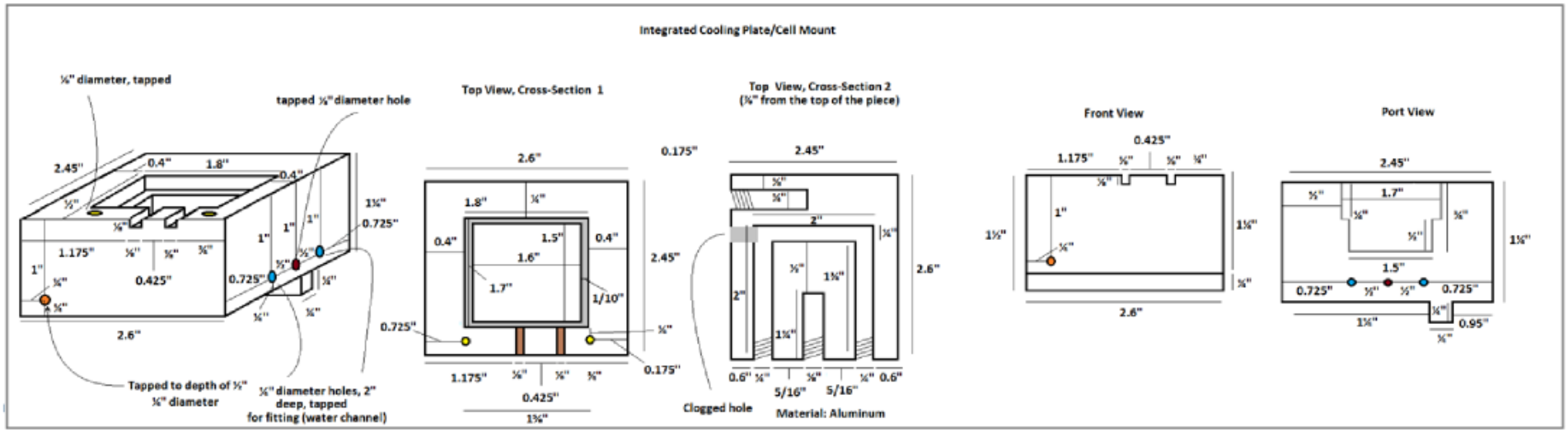

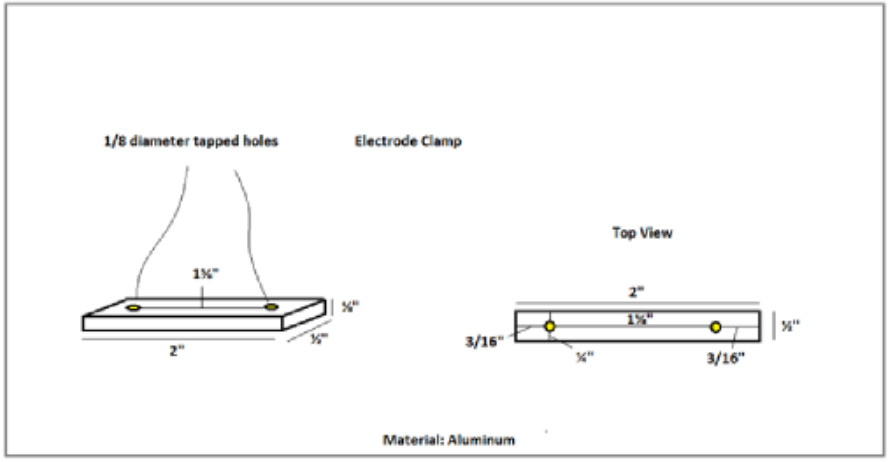

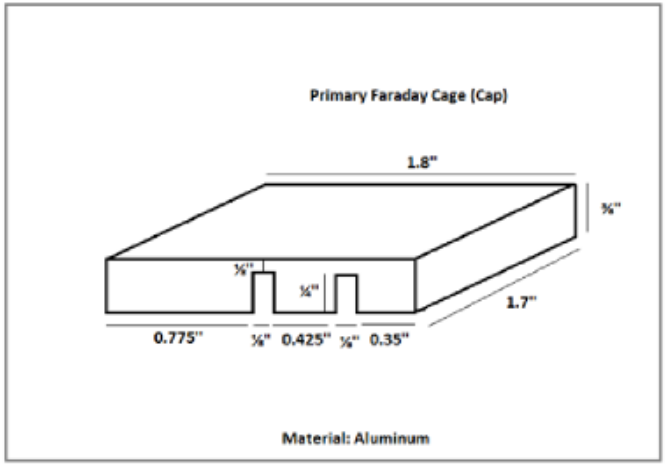

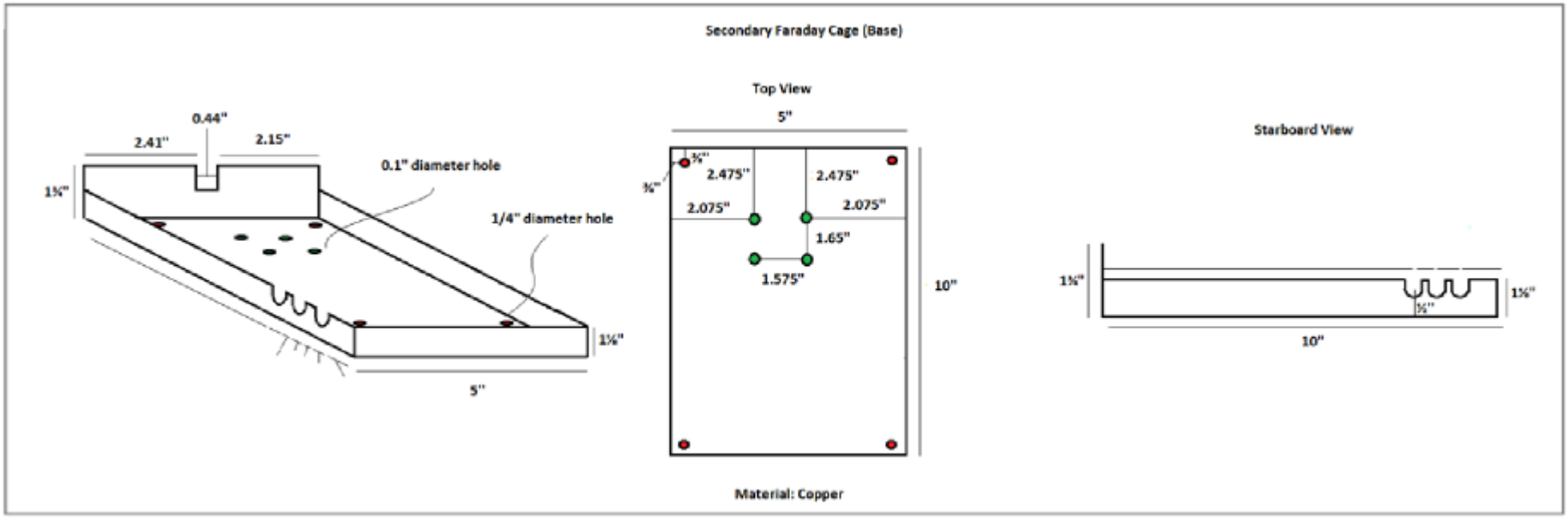
Secondary Faraday Cage (Base)
Top View
Starboard View
0.44"
2.41"
2.15"
0.1" diameter hole
1/4" diameter hole
1¾"
1½"
5"
5"
2.475"
2.475"
2.075"
2.075"
1.65"
1.575"
10"
1½"
1½"
10"
Material: Copper

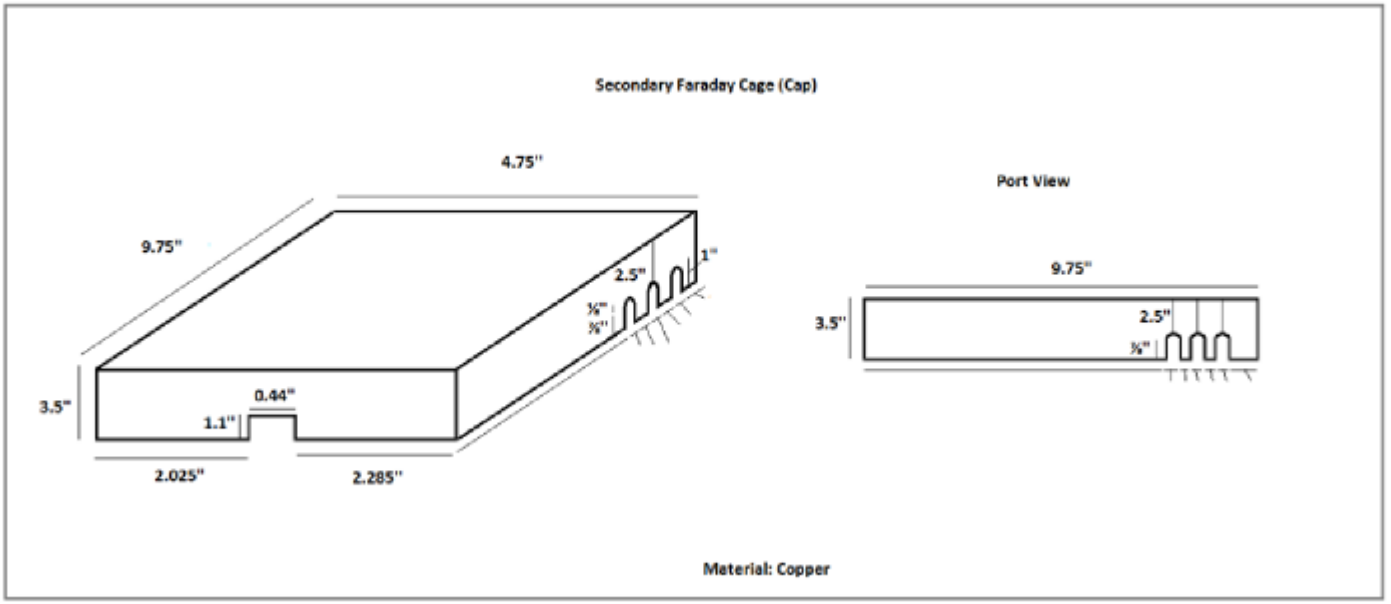
Secondary Faraday Cage (Cap)
4.75"
9.75"
Port View
1"
2.5"
3.5"
0.44"
1.1"
2.025"
2.285"
9.75"
3.5"
2.5"
Material: Copper

Acrylic Base

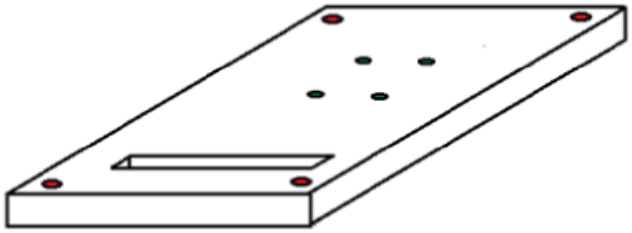

Top View

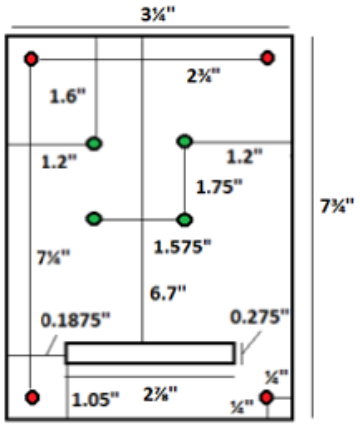

Cross-Sectional Side View

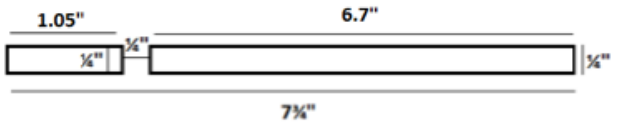

**Compare with Headstage

Headstage Platform

Top View

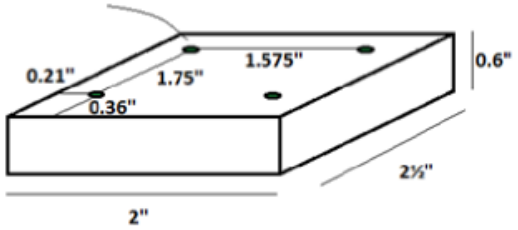

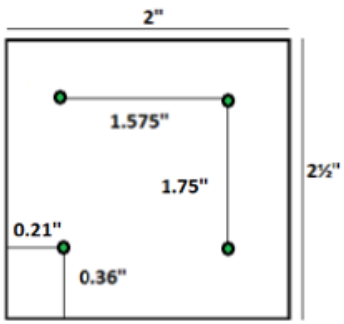

Material: Aluminum

- Headstage Platform Screws
- Acrylic Base Screws
- Water Channels
- Thermostor Cavity
- Grounding Tap
- Electrode Clamp Screws

APPENDIX II – PCR REACTION AND PRIMER DETAILS

Table I PCR primer sequences used to produce 5kb amplicons from λ-DNA.

Primer name	Sequence (5'-3')
Forward primer	Biotin - GTA GTG CGC GTT TGA TTT CC
Reverse primer	Biotin - GTC CAC TGC ATG TTA TGC CG

Table II PCR reaction reagents.

Component	Volume / 50 μL Reaction (μL)	Final Concentration
H_2O	34	
Phusion HF Buffer	10	1X
10 mM dNTPs	1	200 μM each
Primers	2.5	0.2 μM
Template DNA	2	0.02 ng/ μL
Phusion DNA Polymerase	0.5	0.02 Units/ μL

Table III PCR reaction conditions

Cycle Step	Temperature (°C)	Time	Number of Cycles
Initial denaturation	98	1 min	1
Denaturing Annealing Extension	98 64 72	5 s 15 s 1 min 15 s	25
Final extension	72 10	10 min Hold	1